Research Article

Mechanical Responses of a Deeply Buried Granite Exposed to Multilevel Uniaxial and Triaxial Cyclic Stresses: Insights into Deformation Behavior, Energy Dissipation, and Hysteresis

Zhengyang Song [ID],[1,2] **Yunfeng Wu** [ID],[1] **Zhen Yang**,[1] **Xin Cai** [ID],[3] **Yunzhong Jia** [ID],[4] **and Min Zhang**[5]

[1]*Department of Civil Engineering, School of Civil & Resource Engineering, University of Science & Technology Beijing, Beijing 100083, China*
[2]*Xi'an University of Science and Technology, State Key Laboratory of Coal Resources in Western China, Xi'an 710054, China*
[3]*School of Resources and Safety Engineering, Central South University, Changsha, Hunan 410083, China*
[4]*Department of Earth Sciences, Uppsala University, Uppsala 75236, Sweden*
[5]*Geotechnical Institute, TU Bergakademie Freiberg, Freiberg 09599, Germany*

Correspondence should be addressed to Zhengyang Song; zhengyangsong@ustb.edu.cn and Yunfeng Wu; d202110011@ xs.ustb.edu.cn

This article presents the results for cyclic uni/triaxial tests on the deeply seated granite samples drilled from a −915 m deep tunnel in Sanshandao (SSD) gold mine. The monotonic and cyclic tests were carried out to observe the mechanical responses of the granite samples under different loading regimes. The disparities concerning the strain evolution and compressive strength of granite samples considering monotonic and cyclic uniaxial and triaxial loading are presented. Deformation behaviour, dissipated energy, and hysteresis are documented and evaluated. Quantitative correlations between strain evolution and cyclic stress levels are revealed. The amount of energy transformation during uniaxial and triaxial cyclic loading is determined. The impacts of confining pressure level on ultimate strain, energy dissipation, and stress-strain phase shift are presented. The mechanical responses of the granite samples subjected to different stress paths and loading strategies are summarised, and corresponding interpretations are given to clarify the differences of mechanical behaviour encountered in distinct loading methods.

1. Introduction

Cyclic stress is extensively involved in civil engineering and mining procedures; the blasting, hydraulic fracturing, borehole drilling, and periodic excavations in underground space will give rise to chronic and intermittent vibrations, which are often associated with appearance of repeated loads [1, 2]. Cyclic loading has direct impacts on the stability of surrounding rocks and can result in the sudden failure of the rock mass [3–8]. Various mechanical properties, such as elastic modulus [9–12], shear modulus [13, 14], ultrasonic wave velocity [2, 15], and the material strength [16–19], are all found to be degraded with loading duration when exposed to the cyclic stress. The weakening effect due to cyclic loading is in favor of triggering serious dynamic rock disasters, including the rockburst [20–22] and coal burst [23, 24]. Granitic rock masses are frequently encountered in deep mining and utilization of underground space for different purposes [25–27]. This kind of rock has high potential to store abundant of elastic energy owing to the high strength and stiffness [28, 29]. Once rock failure occurs, a large amount of elastic energy stored inside such brittle hard rocks will be released in a violent manner and pose serious threats on personnel safety and infrastructure. Mining induced

stresses are dynamic and cyclic in essence [30–35]. This indicates that cyclic loading should be carefully considered by investigating failure mechanisms of deeply buried rocks in mining and civil engineering. Studies about rocks and other brittle materials prove that cyclic loading significantly impacts the mechanical behaviour during the loading based on insights of material strength, energy dissipation, fracture evolution, permeability, and deformation behaviour [36–38]. Heap et al. [11] state that a stepwise increased cyclic loading leads to progressive degradation of the elastic modulus and a gradual rise of Poisson's ratio based on the tests on a volcanic basalt. Liu et al. [18] document that triaxial cyclic loading shows a weakening effect on dolomite strength by 29.8%–39.9% in comparison with monotonic triaxial compressive strength. Liu and He [39] point that the confinement in cyclic loading will result in wider shear bands compared with the unconfined cyclic loading. Yang et al. [40] experimentally investigated the mechanical responses of the yellow sandstones in triaxial monotonic and cyclic loading, and it is observed that the strengths of yellow sandstones in triaxial cyclic loading do not exhibit an obvious decline compared with the monotonic loading, this is distinct with the strength degradation commonly reported in uniaxial tests. Mitchell and Faulkner [41] state that the sharp rise of permeability for crystalline rocks during the triaxial cyclic loading can effectively indicate the following failure of rocks. Own former tests [15] also document that the stress path has a significant impact on dissipated energy of brittle rocklike materials under uniaxial cyclic loading: a reduction of bottom stress limit in cyclic loading corresponds to a longer fatigue life compared with the stress path when minimum stress is fixed, and the maximum stress is increased. During the mining process, ongoing excavation steps lead to periodic exposure of rocks with corresponding cyclic stress redistributions. This means that the surrounding rocks periodically experience unconfined and confined stress states [42, 43]. Therefore, the mechanical behaviours of the deeply buried brittle rocks subjected to the uni/triaxial stress state are of great significance to study and reveal the damage mechanism of deep hard rocks when the mining induced stress is considered, and the blasting and hydraulic fracturing can both obviously generate the seismic wave, which is accompanied by the cyclic stresses.

This work presents experimental investigation on the mechanical responses of granitic rock samples exposed to uniaxial and triaxial cyclic loading. The samples are drilled from a −915 m deep tunnel in the Sanshandao (SSD) gold mine, which is located in the north eastern coastal area of Shandong province, China. Dynamic events, such as rib spalling and roof fall, are frequently reported during the excavation of this tunnel over the last 2 years. In situ stress monitoring stations installed at this −915 m deep tunnel show that the stress frequently fluctuates during excavation and blasting stages. Considering the actual in situ stress pattern, corresponding cyclic tests were conducted in the laboratory and deformation behaviour, and energy balances and stress-strain phase shift (hysteresis) are investigated using rock samples subjected to different axial stress levels and confinements.

2. Experimental Setup

2.1. Sample Preparation.
The SSD gold mine is located in the north eastern part of Shandong province, China, in the coastal region of Bohai sea. To guarantee reproducibility and comparability, the granite samples are drilled from intact (undisturbed) rock mass (see Figure 1(a)) without any visible cracks. The drilled rock cores are then processed according to ISRM recommendations. The cylindrical specimen has a length of 100 mm and a diameter of 50 mm. All samples were dried at least 72 hours inside a vacuum oven at 40°C. **X**-**R**ay **F**luorescence (XRF) analysis was performed to determine the compositions of the granite (see Table 1 and Figure 1(b)). SiO_2 occupies more than 72% percent, which indicates that sample behaviour is characterized by brittleness, high stiffness, and pronounced hardness.

2.2. Test Apparatus.
The GAW-2000 loading system is used for uniaxial testing (see Figure 2(a)). This system with maximum loading capacity of 2000 kN is capable of performing monotonic and cyclic loading. Figure 2(b) shows the setup of a sample together with the strain measuring system for uniaxial testing. The noncontact CD3755-100 linear variable differential transformer (LVDT) is applied to monitor the axial strain. The radial strain is measured by a strain chain gauge attached at the middle part of the sample. The LVDT can make sure that the stress and strain are synchronous and without any time shift; if the strain gauges are used, it is extremely hard to realize the synchronization of the strain and stress. Figure 2(c) illustrates the triaxial loading system TAW-2000. This system has an axial loading capacity up to 2000 kN. The piston stroke length can reach 200 mm. The maximum confining pressure is 60 MPa. The strain measuring system used for triaxial testing is the same as that used for uniaxial testing. Figure 2(d) shows the layout of the strain measuring system for triaxial testing. The sample is wrapped by a heat shrinkable tube to isolate the sample from the oil (see Figure 2(d)).

2.3. Loading Schemes.
Eight granite samples (#1–#8) are used for uniaxial testing. #1–#3 are monotonically loaded with a rate of 2 mm/min. The axial stress rate approximately ranges between 0.15 and 0.25 MPa/s. Monotonic quasistatic uniaxial tests are performed to determine the uniaxial compressive strength (UCS) of the granite samples. The UCS values act as reference for designing the stress levels for the cyclic tests. #4–#8 are cyclically compressed according to distinct stress paths (see Figure 3). The difference in stress levels between two consecutive cyclic loading stages (CLS) is set to 15 MPa. Loading and unloading rates in each CLS are equal and fixed to 0.75 MPa/s. The lower limits of the stress (minimum stress) are set to zero for all used samples. The cycle number in each CLS for different samples varies (refer to Figures 3(d)–3(h) for uniaxial testing: 1 cycle is used for #4 in each CLS; 3 cycles for #5; 5 cycles for #6; 7 cycles for #7; 9 cycles for #8). Eight granite samples (#9–#16) are used for triaxial testing: #9–#12 are monotonically loaded with
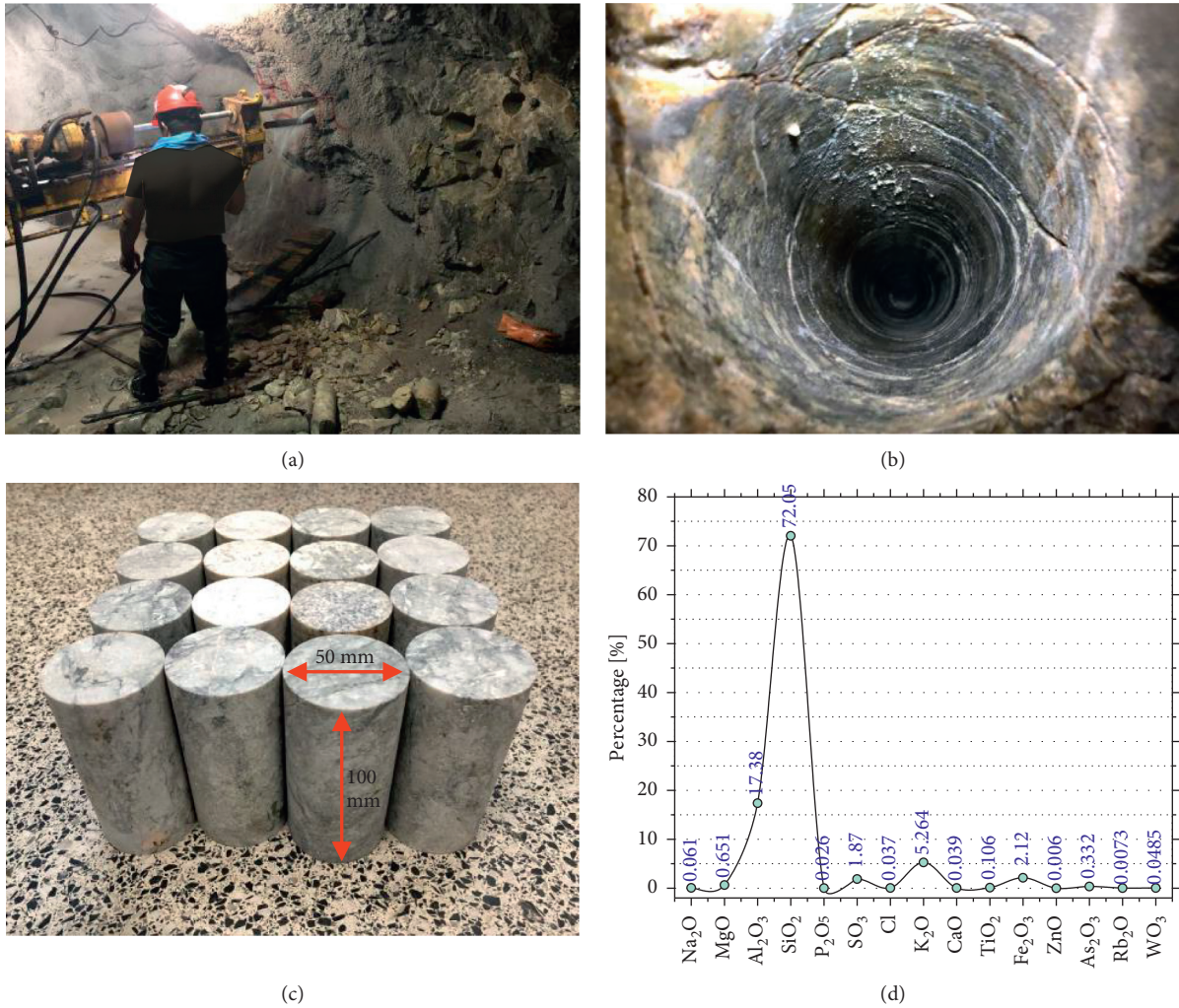
(a)

(b)

(c)

(d)

Figure 1: (a) Rock drilling in SSD gold mine at −915 m-level tunnel. (b) Drilled borehole. (c) Prepared granite samples. (d) Elemental composition of granites based on XRF analysis.

Table 1: XRF analysis: compositions of granites used in laboratory testing (average values).

Na$_2$O (%)	MgO (%)	Al$_2$O$_3$ (%)	SiO$_2$ (%)	P$_2$O$_5$ (%)	SO$_3$ (%)	Cl (%)	K$_2$O (%)	CaO (%)	TiO$_2$ (%)	Fe$_2$O$_3$ (%)	ZnO (%)	As$_2$O$_3$ (%)	Rb$_2$O (%)	WO$_3$ (%)
0.061	0.651	17.38	72.05	0.026	1.87	0.037	5.264	0.039	0.106	2.12	0.006	0.332	0.0073	0.0485

different confining pressures (10 MPa, 15 MPa, 20 MPa, and 25 MPa). #13–#16 are cyclically loaded with the same confinements as used for triaxial monotonic tests. As shown in Figure 3, 5 cycles are used in each CLS, and the difference of maximum stress between two consecutive CLS is 15 MPa. The axial loading rate in triaxial monotonic tests is around 0.1 MPa/s. In triaxial cyclic tests, the loading and unloading rates are both 0.75 MPa/s.

3. Test Results

3.1. Impact of Loading Regimes on Granite Strength and Stress-Strain Relations.
According to axial stress at failure as documented in Figure 3, results of compressive strengths for all 16 granite specimens subjected to different loading

regimes are presented in Figure 4(a). As shown in Figure 4(b), a reduction of average compressive strength is observed for samples that experienced uniaxial loading when monotonic loading shifts to cyclic loading. This indicates the weakening induced by cyclic loading under uniaxial stress. This weakening effect is also reported for different types of rocks under unconfined loading scenarios [17, 44, 45]; see Figures 4(c) and 4(d). Our tests indicate a slight enhanced average compressive strength (152.5 MPa) when exposed to cyclic loading compared with triaxial monotonic loading (132.25 MPa). However, the data base is not sufficient to draw a final or a quite general conclusion. Figures 4(e) and 4(f) show the triaxial compressive monotonic and cyclic strengths of rocks from the published literature [32, 40, 46–49]. In contrast to the unconfined loading

(a)   (b)   (c)   (d)
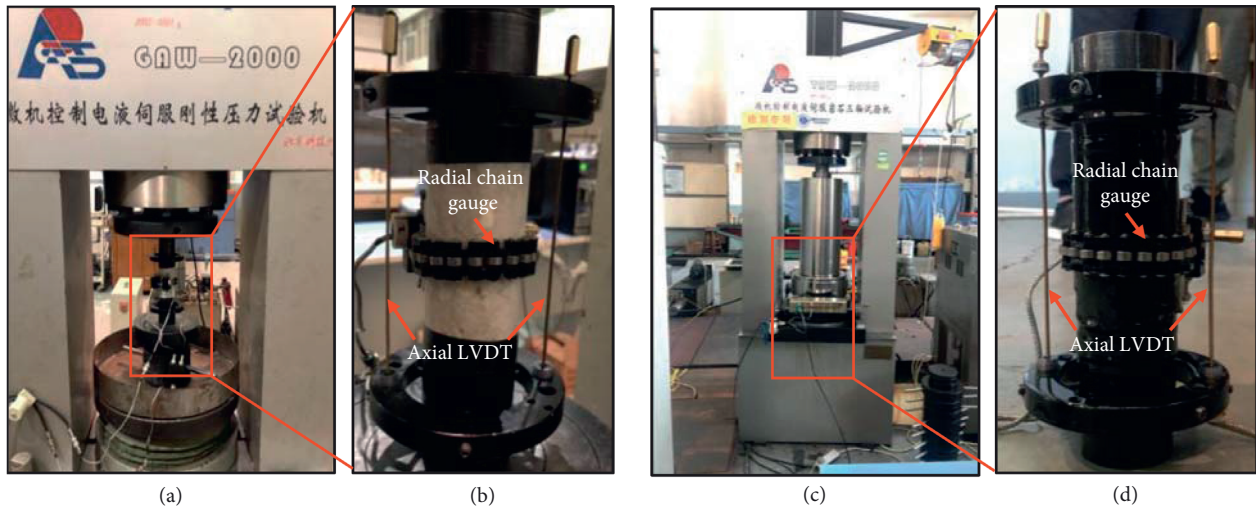
FIGURE 2: Testing device and sample setup: (a) GAW-2000 loading system for uniaxial test; (b) setup of a granite sample for uniaxial test; (c) TAW-2000 loading system for triaxial test; (d) setup of a granite sample for triaxial test.
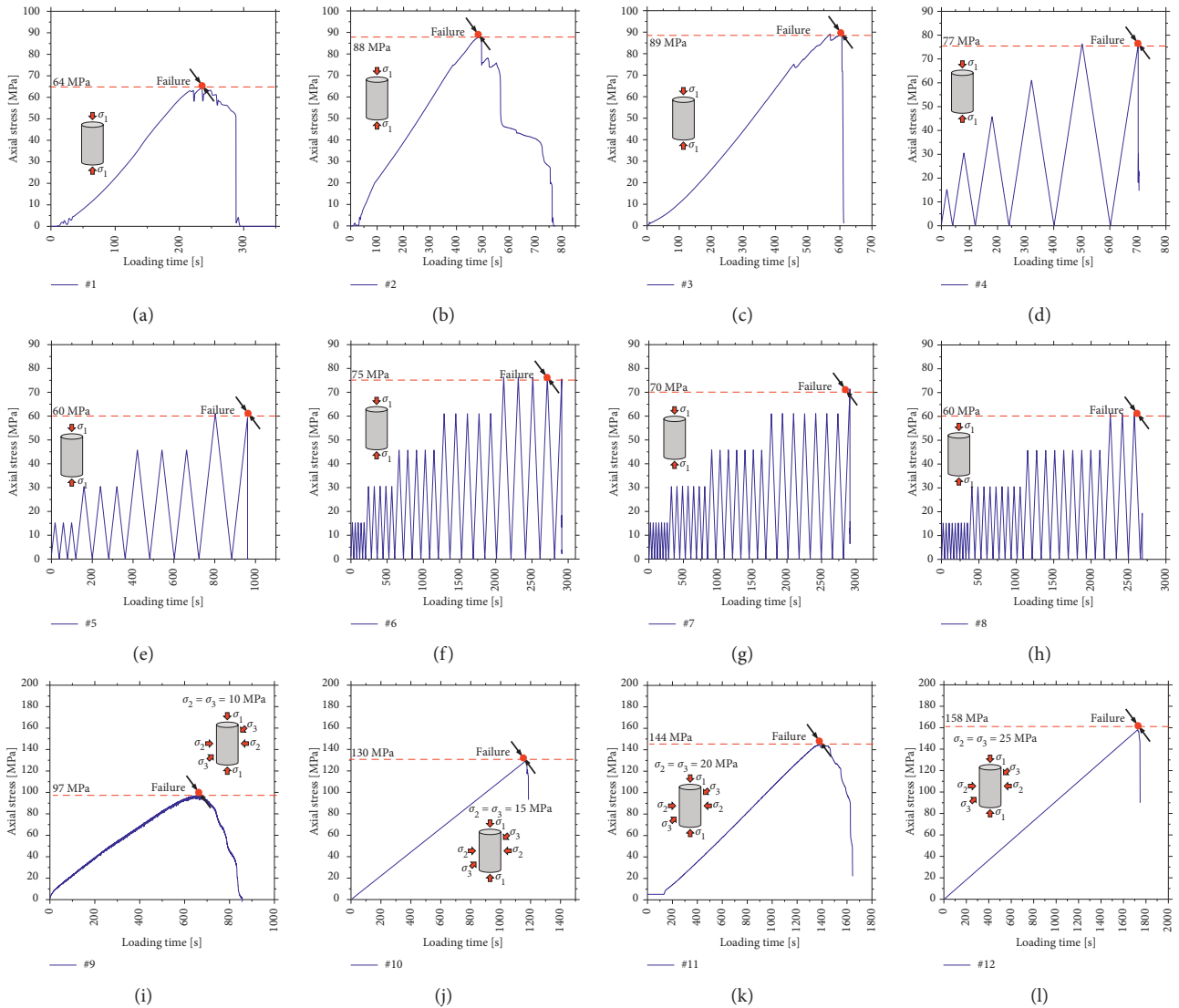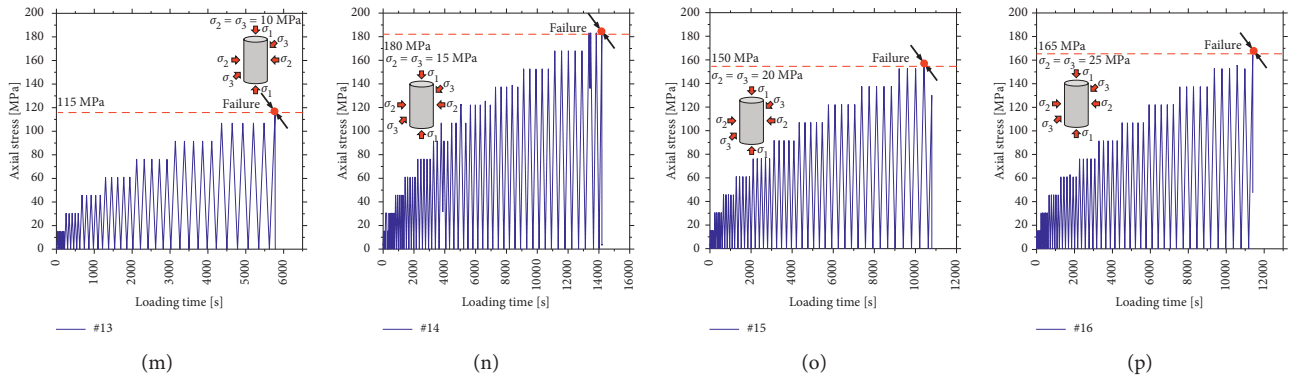

(a) (b) (c) (d)

(e) (f) (g) (h)

(i) (j) (k) (l)

FIGURE 3: Continued.

FIGURE 3: Stress paths in uniaxial tests. (a) #1 monotonic loading. (b) #2 monotonic loading. (c) #3 monotonic loading. (d) #4 cyclic loading, 1 cycle in each level. (e) #5 cyclic loading, 3 cycles in each level. (f) #6 cyclic loading, 5 cycles in each level. (g) #7 cyclic loading, 7 cycles in each level. (h) #8 cyclic loading, 9 cycles in each level. Stress paths in triaxial tests. (i) #9 monotonic loading, confinement 10 MPa. (j) #10 monotonic loading, confinement 15 MPa. (k) #11 monotonic loading, confinement 20 MPa. (l) #12 monotonic loading, confinement 25 MPa. (m) #13 cyclic loading, confinement 10 MPa. (n) #14 cyclic loading, confinement 15 MPa. (o) #15 cyclic loading, confinement 20 MPa. (p) #16 cyclic loading, confinement 25 MPa.
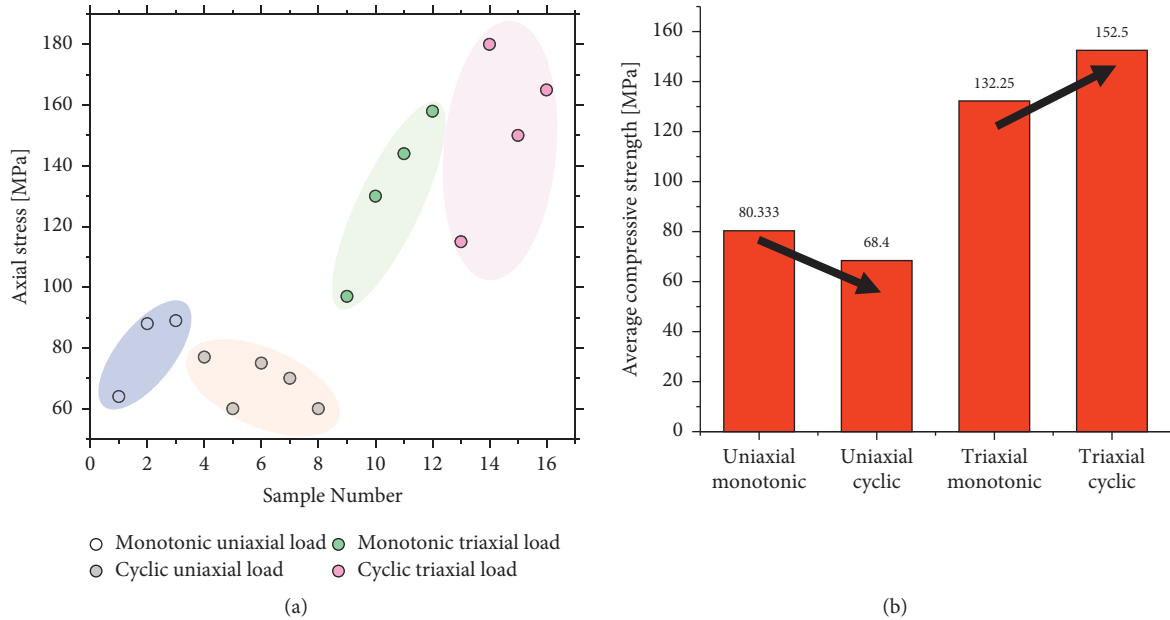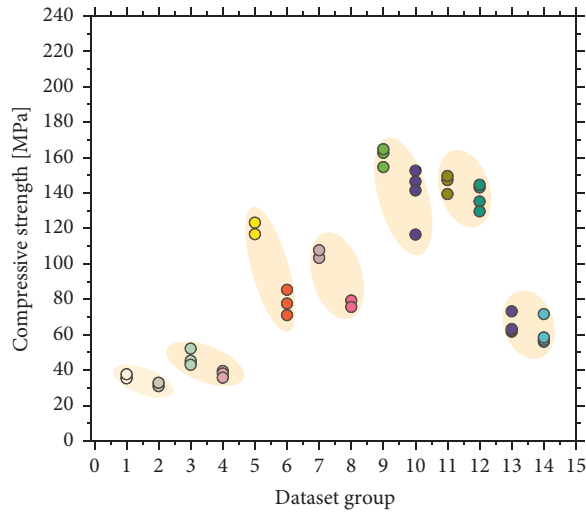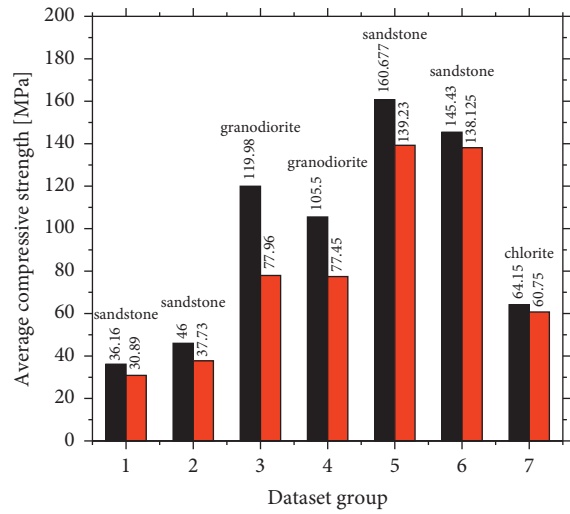

FIGURE 4: Continued.
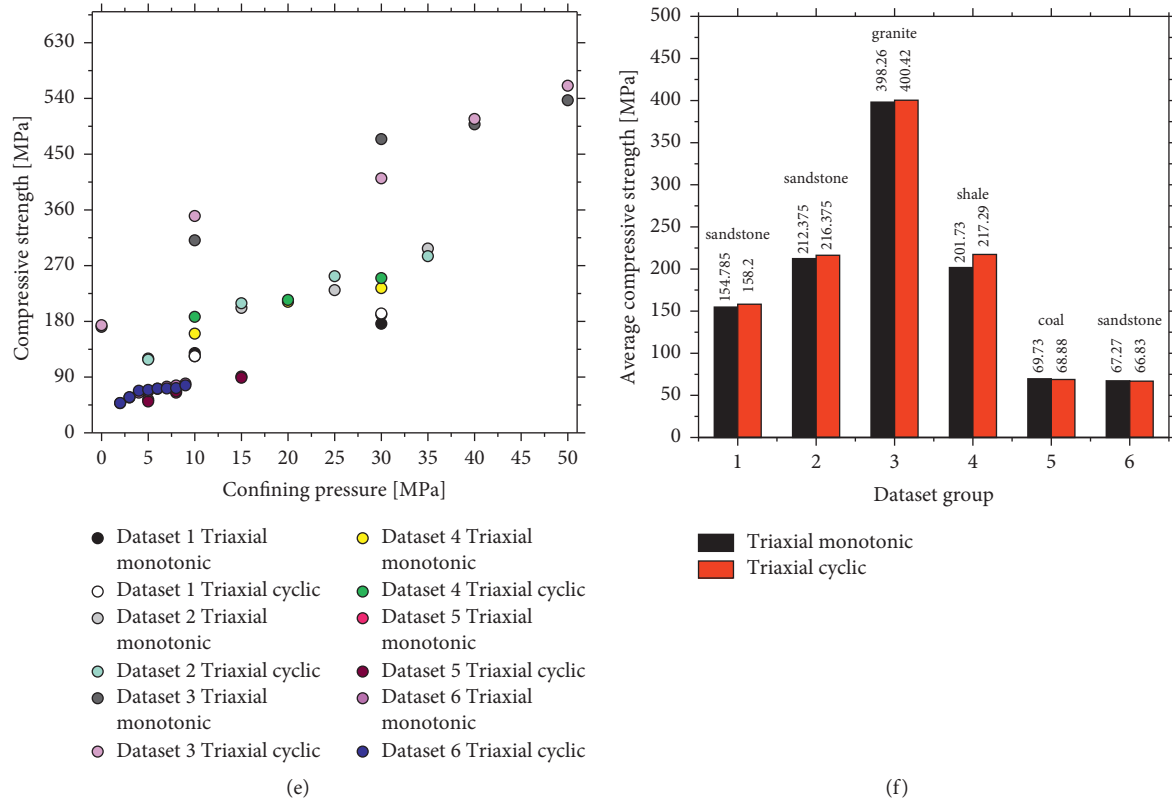
(c)

(d)

Figure 4: Continued.

(e)

(f)

Figure 4: (a) Compressive strength for all 16 tested granite samples. (b) Average compressive strength obtained from uniaxial and triaxial tests; uniaxial testing data from published literature. (c) Uniaxial compressive strength under monotonic and cyclic loading. (d) Average compressive strength under monotonic and cyclic loading: datasets 1–4 from [17]; datasets 5-6 from [44]; datasets 7 from [45]; triaxial testing data from published literature. (e) Triaxial compressive strength under monotonic and cyclic loading. (f) Average compressive strength under monotonic and cyclic loading: dataset 1 from [40]; dataset 2 from [46]; dataset 3 from [32]; dataset 4 from [47]; dataset 5 from [48]; dataset 6 from [49].

scenario, under triaxial compression, the cyclical loaded samples show the same or even slightly higher compressive strength compared to monotonic loading. The published datasets as well as our experimental results indicate that cyclic loading may not exert a dominant impact on strength degradation when the confinement is applied.

The stress-strain curves for all tested 16 granite samples are shown in Figures 5 and 6. Figure 5 shows the stress-strain curves from uniaxial tests. All 8 figures show that the volumetric strains under uniaxial conditions are dominated by compressive axial strain irrespective of whether monotonic or cyclic loaded. As indicated by the volumetric strains (blue curves) in Figure 5, no volume dilation occurs prior to final failure of the samples. This behavior coincides with the rupture behavior of brittle hard rocks subjected to uniaxial compressive loading [29, 50]. Dilation is only notable in the postpeak region.

Figure 6 shows stress-strain curves obtained from triaxial tests. Due to the application of confining pressure, dilatancy occurs much earlier (see blue lines in Figure 6). The onset of dilatancy is often used as precursor to predict failure [51], and dilatancy criteria have become important for the design of underground structures [52, 53]. The impact of confinement on rock dilatancy exposed to

monotonic loading is extensively investigated and summarised in many published articles [54, 55]. In our study, we applied the same confining pressure for monotonic and cyclic loaded samples to observe the effect of confinement on the two different loading regimes. Figures 6(a)–6(d) show the stress-strain curves obtained from triaxial monotonic loading, and Figures 6(e)–6(h) show the results from triaxial cyclic loading. The axial stresses at minimum volumetric strain (green points in Figure 6) and at the onset of rock dilatancy (red points in Figure 6) are recorded. The rocks are typical brittle materials with abundance of voids and inherent fractures. If no confinement is applied, the rupture of rock is totally violent and abrupt, almost with no plastic deformation due to the lack of resistance to shearing. For a higher confinement case, the shear force exceeds the cohesions between the grains, causing the cohesive particles to fracture. The application of the confinements ($\sigma_2 = \sigma_3$) will laterally resist the sliding of fractured rock fragmentation along the formed fractures directions. The larger the confinement is, the more sliding and shear fracturing can be resisted, and this will lead to a huge shear band, which finally results in the dilation of rocks. To sum up, the obvious dilation of the rock sample under higher confinement is due to more generated
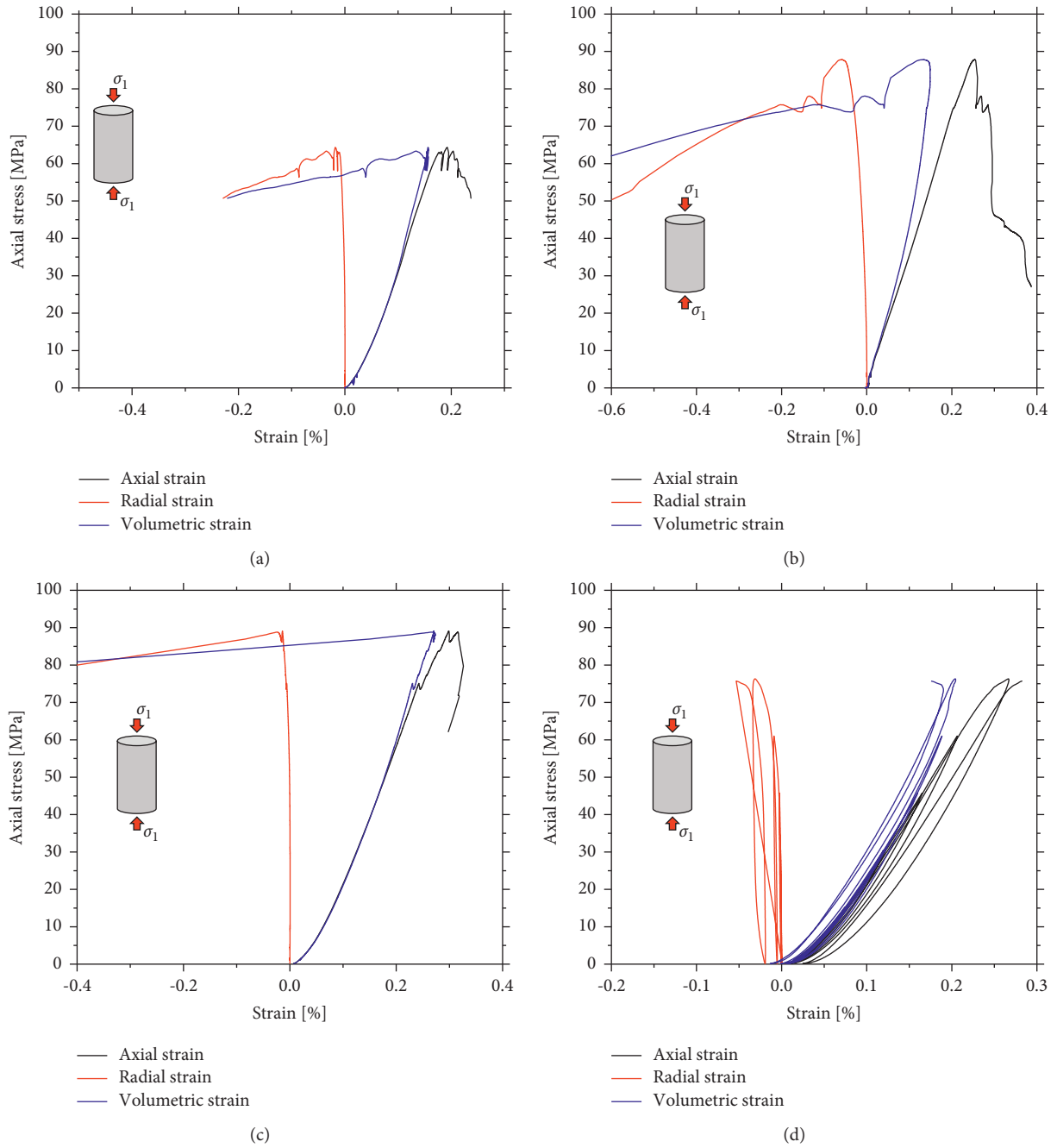
(a)

(b)

(c)

(d)

Figure 5: Continued.
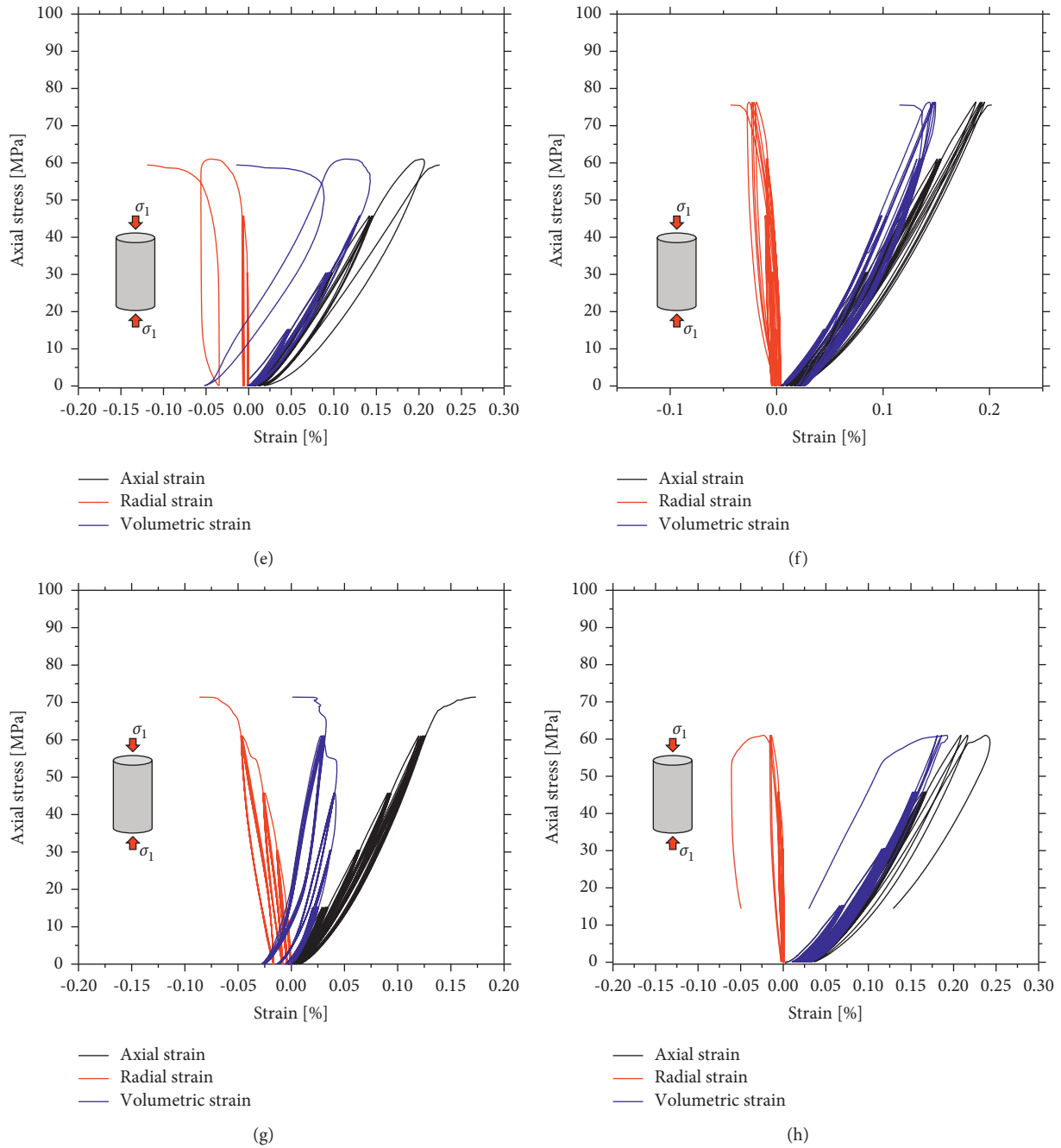
(e)

(f)

(g)

(h)

FIGURE 5: Stress-strain curves in uniaxial tests. (a) #1 monotonic loading. (b) #2 monotonic loading. (c) #3 monotonic loading. (d) #4 cyclic loading, one cycle in each level. (e) #5 cyclic loading, 3 cycles in each level. (f) #6 cyclic loading, 5 cycles in each level. (g) #7 cyclic loading, 7 cycles in each level. (h) #8 cyclic loading, 9 cycles in each level.

fractures and cracks, and the higher confinement will more strongly stabilize the rock samples.

Figure 7 presents the correlation between confining pressure and axial stress when minimum volume and rock dilatancy appears. The data remarked with zero confinement are selected from Figure 5(f) corresponding to the uniaxial test results of #6. The axial stress path for #6 is the same as used in triaxial testing. Therefore, the data for #6 is compatible with the triaxial test results shown in Figure 7 making the dataset more robust and comprehensive. Figure 7 shows that the ratios of axial stress/peak stress at the points of minimum volume and onset of dilatancy both decline with increasing confinement. To sum up, confining pressure leads to a more pronounced rock dilation prior to failure in case of cyclic as well as monotonic loading. A larger confinement allows a more pronounced rock dilation regardless whether monotonic or cyclic loading is applied. The possible interpretations for different stress ratios can be from two perspectives:
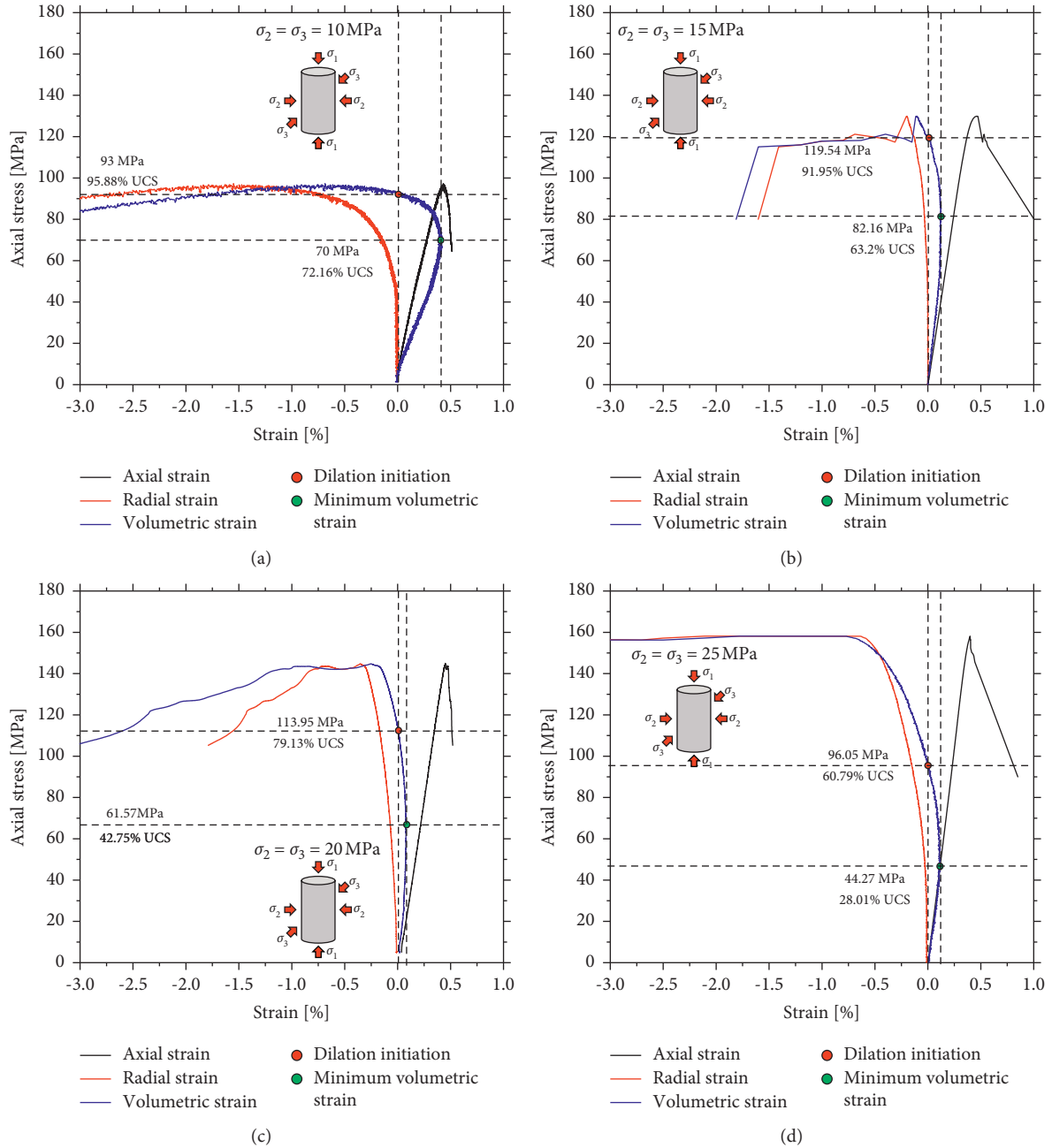
(a)

(b)
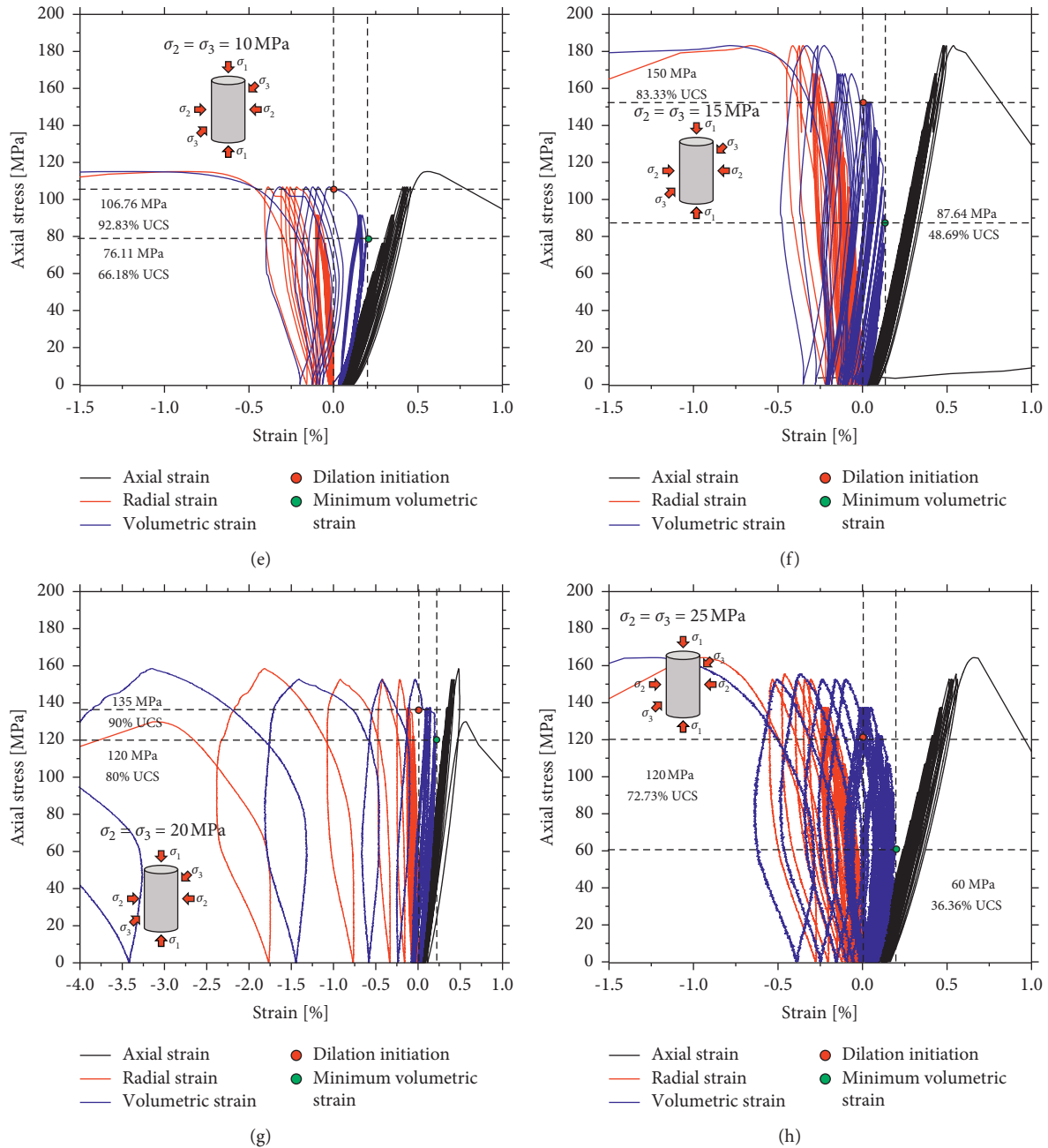

(c)

(d)

Figure 6: Continued.

Figure 6: Stress-strain curves in triaxial tests. (a) #9 monotonic loading, confinement 10 MPa. (b) #10 monotonic loading, confinement 15 MPa. (c) #11 monotonic loading, confinement 20 MPa. (d) #12 monotonic loading, confinement 25 MPa. (e) #13 cyclic loading, confinement 10 MPa. (f) #14 cyclic loading, confinement 15 MPa. (g) #15 cyclic loading, confinement 20 MPa. (h) #16 cyclic load, confinement 25 MPa.

(1) The higher confinement is more in favor of the shear cracks' development and coalescence, and the higher confinement can trigger more fractures orientated along the horizontal or quasi horizontal directions, which will accelerate the volumetric dilation and make the dilation appear more earlier.

(2) The "stress ratio" is defined as the stresses at two critical moments (minimum volume and onset of dilation) to the final strength. The high confinement will lead to a significant increase of final strength due

to strain hardening behaviors, and this extraordinary high final strength under larger confinement will also lead to the reduction of the stress ratio.

3.2. Deformation Behaviour. Deformation related parameters like ultimate strains at failure or growth rates of axial strain provide good indicators [15, 56, 57] to characterize the evolution of damage during cyclic loading. This section presents the deformation behaviour of the granite samples under uniaxial and triaxial cyclic loading.
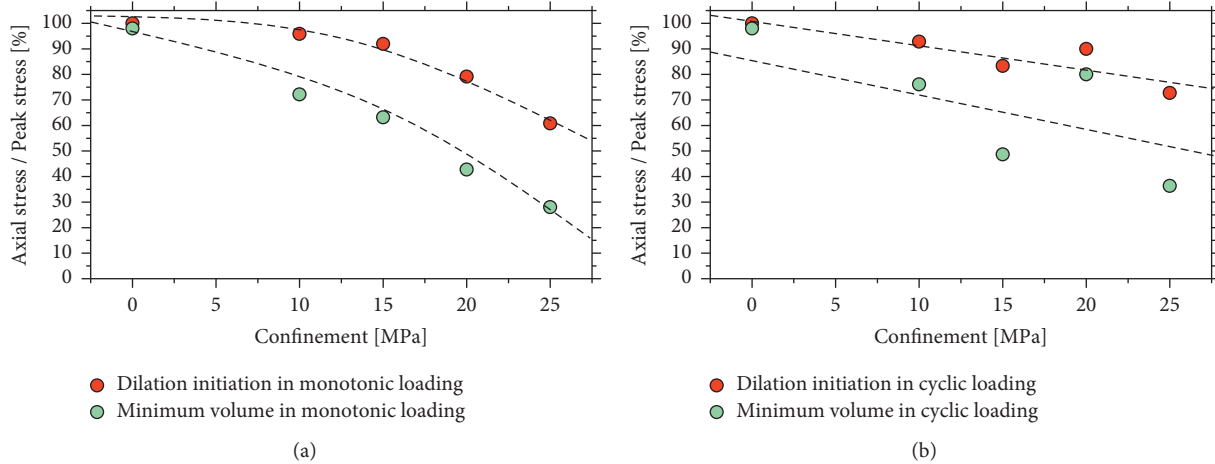
FIGURE 7: Ratio of axial stress/compressive strength at minimum volume and onset of dilation for different confining pressures: (a) triaxial monotonic loading; (b) triaxial cyclic loading.

3.2.1. Impact of Loading Regime on Ultimate Strain at Failure. The ultimate axial, radial, and volumetric strains for the 16 granite samples at peak stress (defined as point of failure) are shown in Figure 8. #1 to #8 are exposed to uniaxial compression, while #9 to #16 are exposed to triaxial compression. Ultimate axial strains for triaxial loaded samples are obviously larger than uniaxial loaded ones (see Figure 8(a)). A similar behaviour is documented in Figure 8(b) for radial strains. Figure 8(c) presents volumetric strains when peak stress is reached. The red horizontal dashed line in Figure 8(c) signifies the borderline between volumetric expansion and compression. #1 to #8 subjected to the uniaxial loading failed in a contraction state, whereas #9 to #16 failed with dilation. These results demonstrate that, for brittle hard rocks like the investigated granite, the samples do not show significant dilatancy at peak stress if they are uniaxially compressed irrespective of monotonic or cyclic loaded. However, dilatancy occurs under monotonic and cyclic loading when confined pressure is applied.

3.2.2. Impact of Confining Pressure on Growth Rate of Strains. Growth rate of strain is a quantitative index to characterize damage. Higher growth rates of strain correspond to a higher degree of damage. Typically for brittle rocks, the axial strain commonly undergoes a steep rise immediately preceding the rupture. Herein, we defined two indexes characterizing the extent of the growth rate. For granite samples exposed to triaxial cyclic loading, 5 cycles are applied in each stress level. The strain rate for each stress level is defined as $(\varepsilon^5 - \varepsilon^1)/5$, where ε^5 and ε^1 are the strains at the 5th and 1st cycles, either measured axially or radially. Usually, strains at maximum and minimum stress are used to characterize the growth rate: the strain rate determined at maximum stress is termed peak strain rate. Correspondingly, the strain rate calculated at minimum stresses is termed residual strain rate. Figure 9 presents peak and residual strain rates versus gradually increased axial maximum stresses for triaxial cyclic loaded samples exposed to different confining pressures. Figures 9(a) and 9(b) show axial strain rates at maximum

and minimum stresses. It becomes obvious that the axial peak and residual strain rate follows a nonlinear relation with respect to the maximum axial stress. For low confinement (e.g., 0 and 10 MPa), the curve is steeper compared to larger confinement (e.g., 15, 20, or 25 MPa). However, as documented by Figures 9(c) and 9(d), the impact of confinement on radial strain rate is not that pronounced compared with axial strain rate. Figure 9 indicates that the effect of confinement on strain growth rate is quite prominent in axial direction, which is parallel to the major principal stress. In summary, a higher axial strain rate under low confining pressures exacerbates the failure of granite samples. This also explains the premature of samples under exposed to lower confinements.

3.2.3. Evolution of Dynamic Secant Elastic Modulus. The elastic modulus is a critical parameter to determine the correlations between stress and strain. The gradual degradation of elastic modulus during uniaxial cyclic loading is extensively reported for geomaterials [11, 13, 58–60]. The deterioration of the stiffness is often associated with the sustaining evolution of cracks inside the rock samples. The evolution of secant elastic modulus for granite samples is illustrated in Figures 10 and 11. The secant modulus is calculated following this equation: $(\sigma_{max} - \sigma_{min})/(\varepsilon_{max} - \varepsilon_{min})$, where σ_{max} and σ_{min} are the maximum and minimum stresses within a cycle, and ε_{max} and ε_{min} are the axial strains corresponding to σ_{max} and σ_{min}, respectively.

Figure 10 shows the evolving of secant modulus versus the cycle number as well as the maximum axial stress for granite samples in uniaxial cyclic testing. It is observed that, with increasing maximum axial stress, the secant elastic modulus of the first cycle undergoes an obvious elevation, and then the secant modulus remains constant or exhibits a slight decline within the current loading stage. This behaviour is verified by all 5 samples documented in Figure 10. This demonstrates that, under uniaxial cyclic loading, the stiffness of granite samples will be slightly enhanced when the stress level is stepwise increased. By approaching failure,
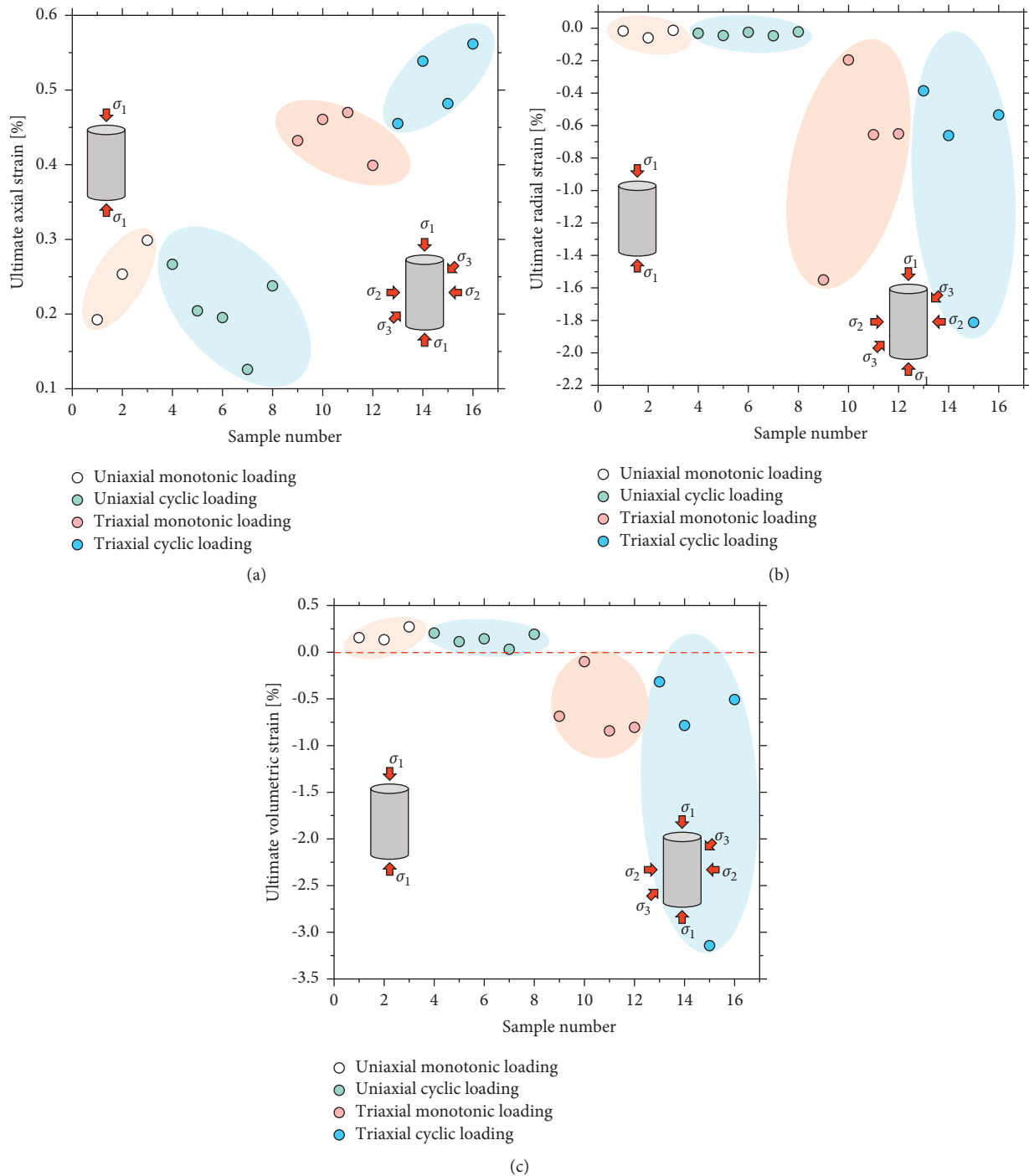
(a)

(b)

(c)

FIGURE 8: Ultimate strain at failure for 16 granite samples: (a) ultimate axial strain; (b) ultimate radial strain; (c) ultimate volumetric strain.

a drastic drop of elastic modulus is captured within 3 or 4 cycles (see areas enclosed by red dashed lines in Figure 10), which signifies a significant loss of stiffness and load bearing capacity. This precursory phenomenon is suited to predict the fatigue failure of rocks under cyclic loading.

The evolution of secant modulus for granite samples under triaxial cyclic loading with different confining pressures is shown in Figure 11. Compared to the Figure 10 (uniaxial loading), the evolution of the secant modulus for

samples exposed to cyclic loading shows a distinct pattern when confinement is higher than 20 MPa (refer to Figures 11(d) and 11(e)). This indicates that the confining pressure has a critical threshold for pattern change. In this work, the threshold is about 20 MPa, which means that the secant modulus will decline with increasing stress level when confinement is larger than about 20 MPa rather than increasing as observed for confinement less than about 20 MPa. Furthermore, under triaxial cyclic loading, a longer
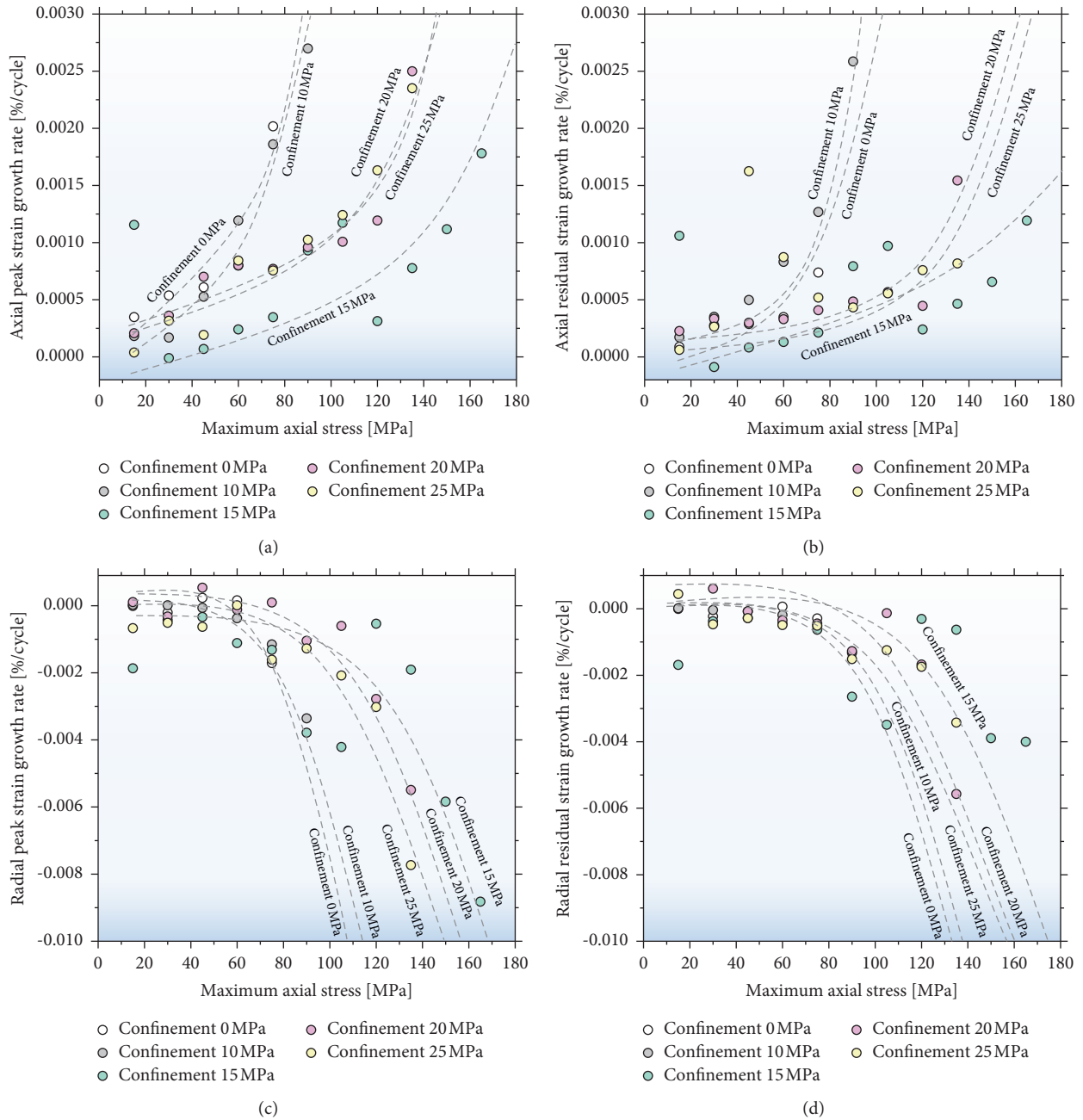
FIGURE 9: (a) Axial peak strain growth rate versus maximum axial stress. (b) Axial residual strain growth rate versus maximum axial stress. (c) Radial peak strain growth rate versus maximum axial stress. (d) Radial residual strain growth rate versus maximum axial stress.

and earlier precursory phase is observed: around 4 to 6 cycles (see blue dashed lines in Figure 11) with obvious drop of secant modulus prior to failure. This indicates that the rupture of granitic rocks under uniaxial cyclic loading is more abrupt than under triaxial cyclic loading.

3.3. Energy Dissipation during Cyclic Loading. The input and dissipated energy during cyclic loading are widely investigated for rock materials [20, 61–64]. The variations of cyclic stress levels lead to different amount of energy exchange during cyclic loading. Usually, three types of energy are

calculated based on the stress-strain curve (hysteresis loop) as illustrated in Figure 12: input energy, elastic recovery energy, and dissipated energy. The dissipated energy is equal to the difference between input and elastic recovery energy. A large amount of dissipated energy is often associated with the high possibility of failure, which signifies pronounced loss of elasticity and substantial damage inside the rock. Many literatures document that dissipated energy increases dramatically for brittle geomaterial immediately preceding failure during cyclic loading [23, 65–67]. Therefore, a fundamental understanding of the energy balance is critical to continuously characterize the fatigue damage. In Figure 12,
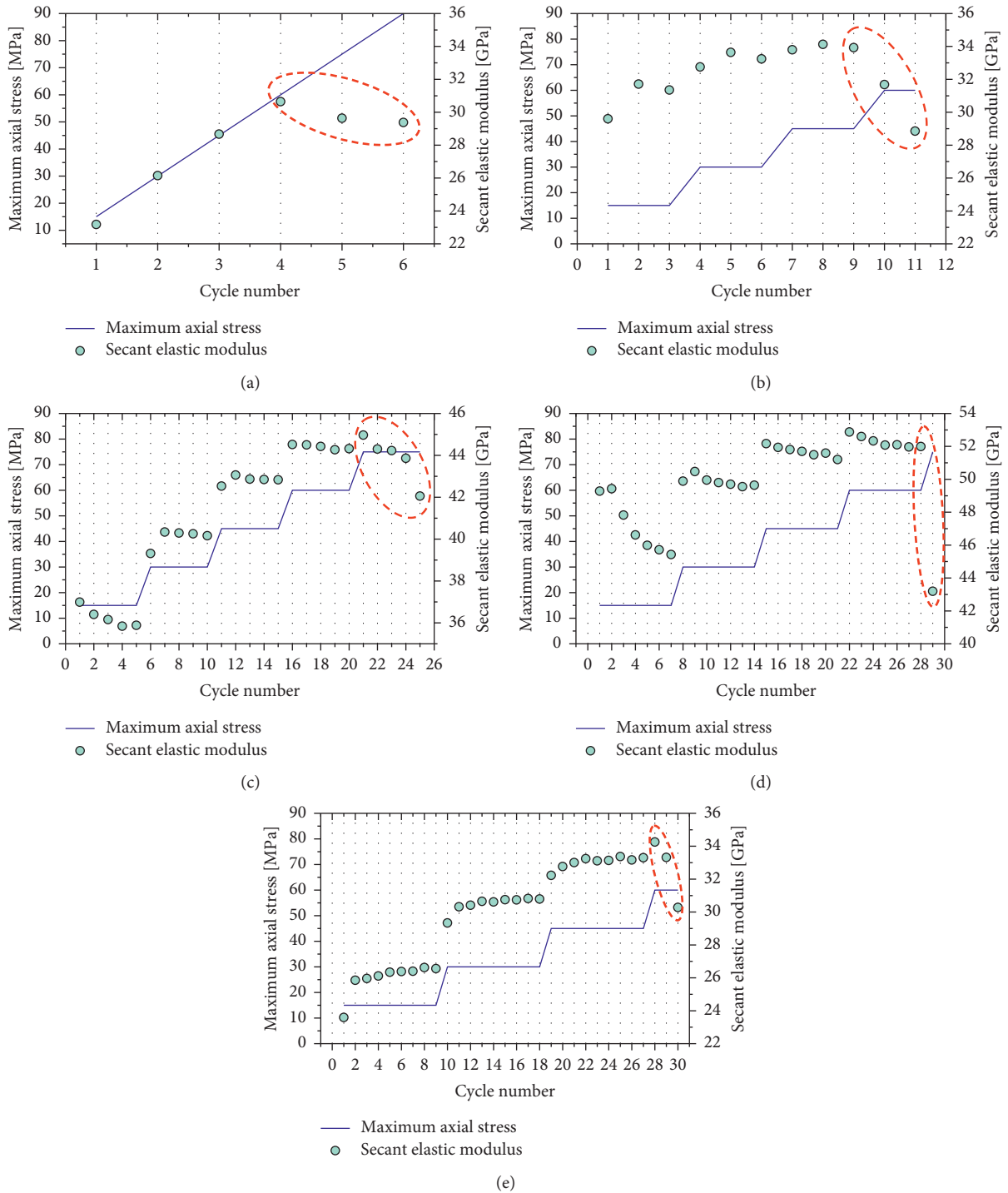
FIGURE 10: Evolution of secant elastic modulus versus cycle number for uniaxial cyclic testing. (a) #4, 1 cycle in each loading level. (b) #5, 3 cycles in each loading level. (c) #6, 5 cycles in each loading level. (d) #7, 7 cycles in each loading level. (e) #8, 9 cycles in each loading level.

the vertical axis is the stress imposed on the rock sample, and the horizontal axis is the axial strain induced; therefore, the unit of the areas under the curve has the unit of J/m^3. This energy is often called "energy density" [35, 63, 68].

Figure 13 illustrates the evolution of the three types of energy density for the samples under uniaxial cyclic loading. Please note that the energy value of the last cycle is excluded

due to the extreme values and inconclusive determination. With the step-wise increase of maximum axial stress, all three types of energy density increase. For samples that experienced at least 3 cycles in each level (see Figures 13(b)–13(e)), the elastic energy density (grey symbols) is almost constant, which indicates that the elastic recovery energy density is dictated by the stress level. For input and
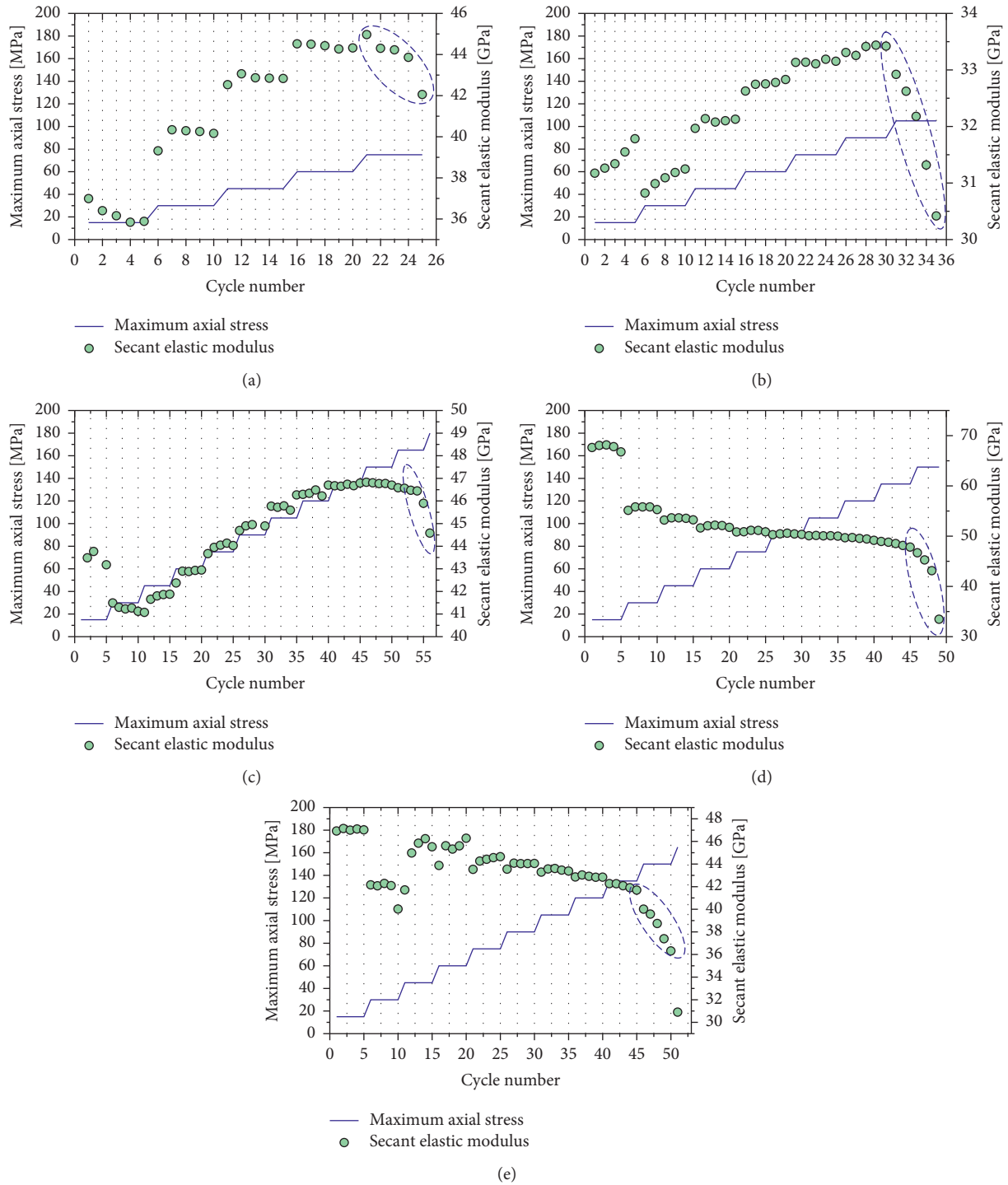
(a)

(b)

(c)

(d)

(e)

FIGURE 11: Evolution of secant elastic modulus versus cycle number for triaxial cyclic testing. (a) #6, no confinement. (b) #13, confinement of 10 MPa. (c) #14, confinement of 15 MPa. (d) #15, confinement of 20 MPa. (e) #16, confinement of 25 MPa.

dissipated energy, the values for the first cycle after stress increase exhibit an obvious growth followed by a slight decline. For #8 (see Figure 13(e)), both input and dissipated energy density values shoot up to a high level just prior to failure, whereas the elastic energy density still remains constant. Figure 13 demonstrates that amounts of input and dissipated energy density drastically raise when approaching

failure, and the substantial damage inside the rocks at failure will result in a dramatic increase of input energy, which is governed by the loss of stiffness. This is consistent with the modulus degradation illustrated in Figure 10. Figures 14(a)–14(c) present the accumulated three types of energy density versus cycle number. Clearly, the total amounts of energy density, regardless of category, are all stress-path-related.
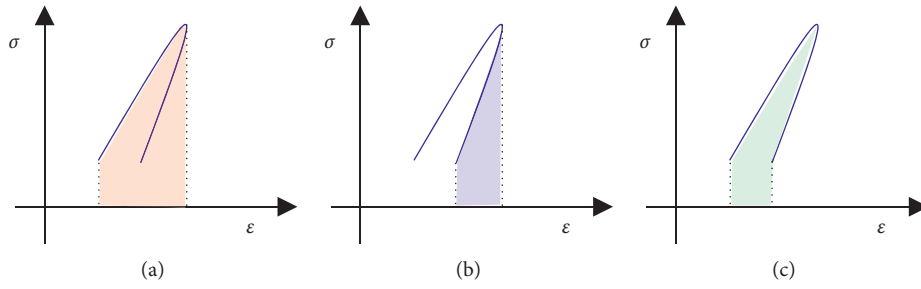
FIGURE 12: Illustration of three types of energy during cyclic loading: (a) input energy; (b) elastic recovery energy; (c) dissipated energy.

FIGURE 13: Continued.

(e)

FIGURE 13: Evolution of energy densities during uniaxial cyclic loading. (a) #4, 1 cycle in each level. (b) #5, 3 cycles in each level. (c) #6, 5 cycles in each level. (d) #7, 7 cycles in each level. (e) #8, 9 cycles in each level.

(a)

(b)

FIGURE 14: Continued.

(c)

(d)

(e)

(f)
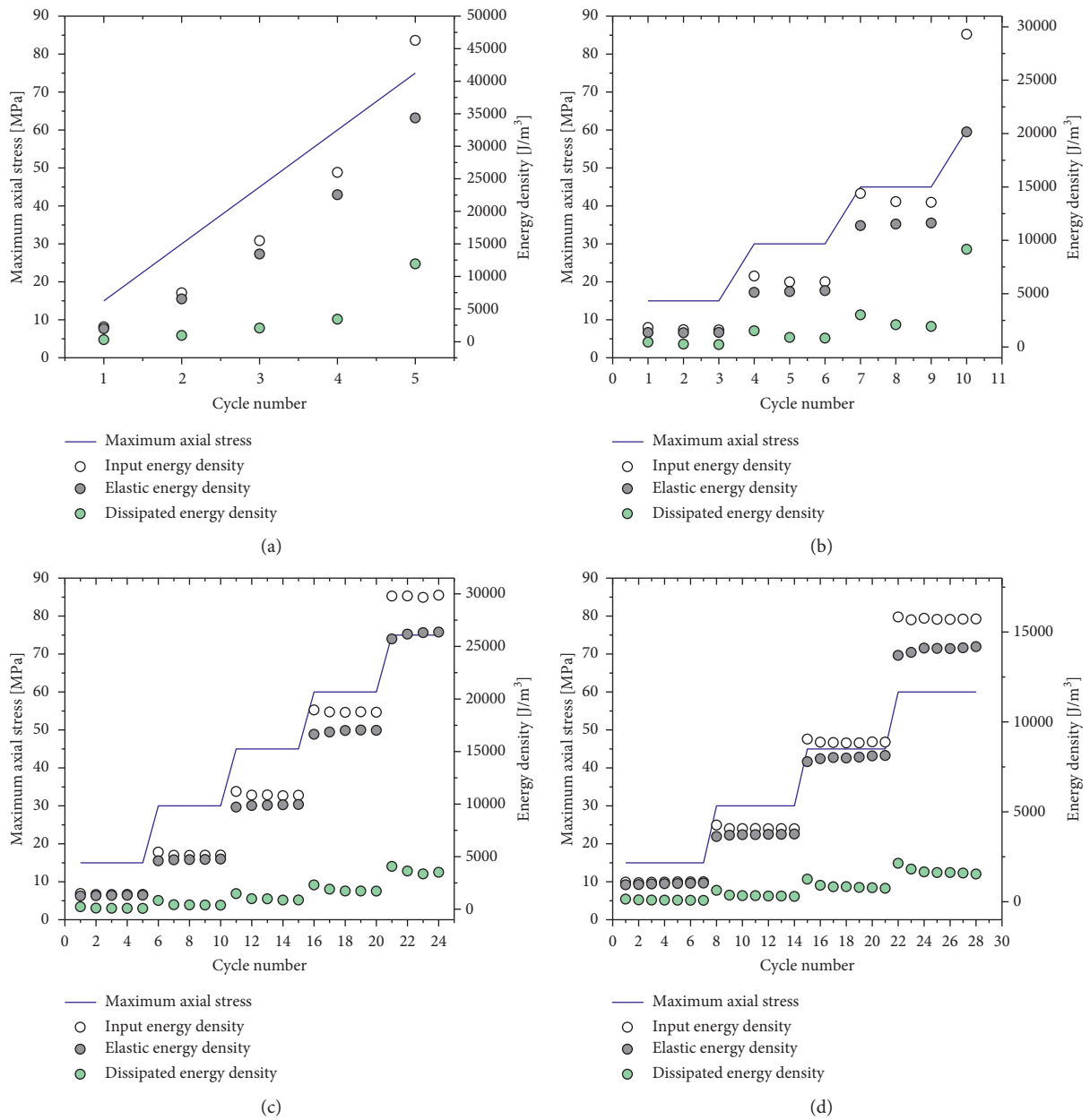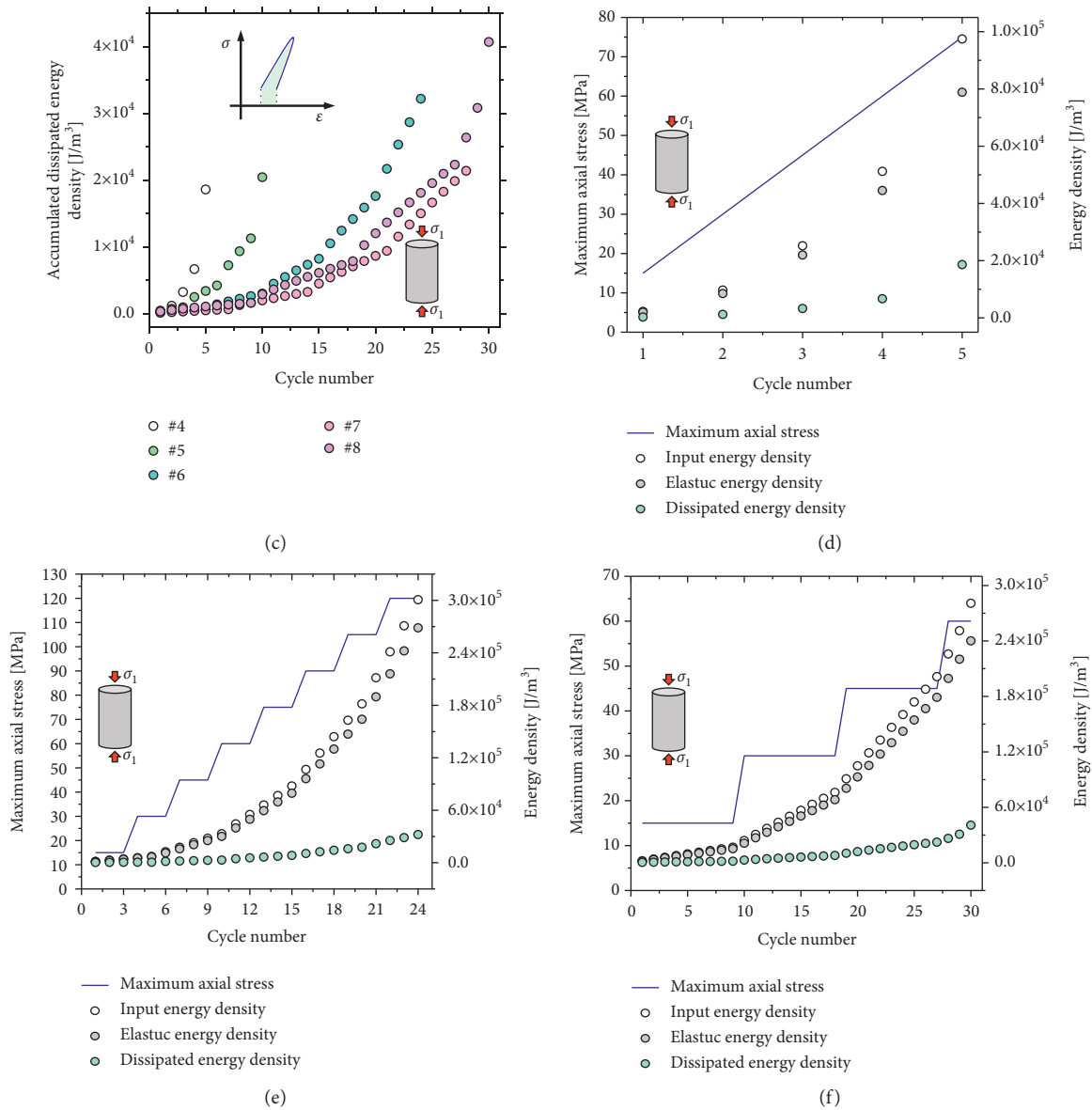
Figure 14: Evolution of accumulated energy densities during uniaxial cyclic loading: (a) accumulated input energy density; (b) accumulated elastic energy density; (c) accumulated dissipated energy density; (d) three types of accumulated energy for #4; (e) three types of accumulated energy for #6; (f) three types of accumulated energy for #8.

For those samples experiencing limited cycles in each load level, for examples #4 and #5 (1 and 3 cycles are applied in each level, respectively), the three types of accumulated energy density all show a lower level at failure compared with the other three samples undergoing more cycles in each load level. More cycles applied at lower stress level cause a larger amount of input and dissipated energy density at failure. This conclusion confirms former lab testing results based on the brittle rocklike materials exposed to the uniaxial cyclic loading [15]. Figures 14(d)–14(f) show all three energy density types plotted together based on #4, #6, and #8. The rise in cyclic load level is connected to an increasing violent energy exchange.

The evolution of energy density versus cycle number as well as axial stress in triaxial cyclic testing is shown in

Figure 15. The stepwise increment of all types of energy density with the rise of axial stress is also observed under triaxial cyclic loading. Distinct from the uniaxial results documented in Figure 13, the amount of elastic recovery energy density (grey symbols) also obviously rises shortly preceding the failure instead of remaining almost constant as under uniaxial cyclic loading. This signifies that the deformation recovery energy during the unloading phase is also increasing with the rise of axial stress when a confinement is applied. The accumulated energy density for the granite samples under triaxial cyclic loading is plotted in Figure 16. Distinct from the nonuniform stress paths under uniaxial cyclic loading (see Figure 13), the stress paths for different granite samples under triaxial cyclic loading are the same; refer to the blue solid lines in Figure 16. Figure 16 shows that
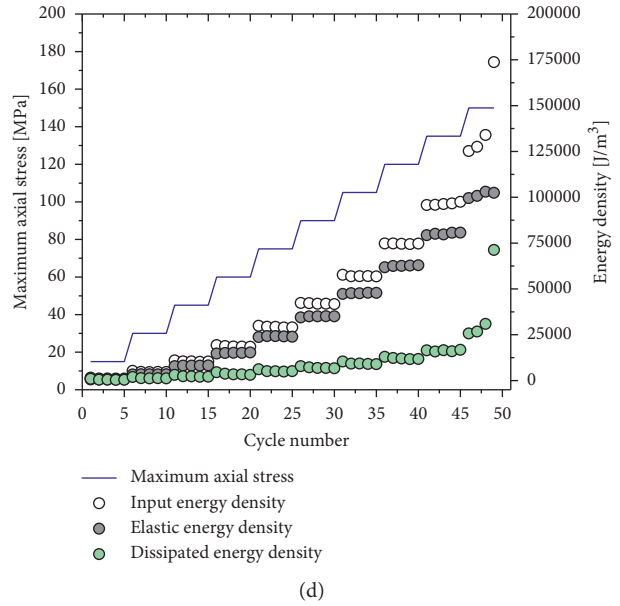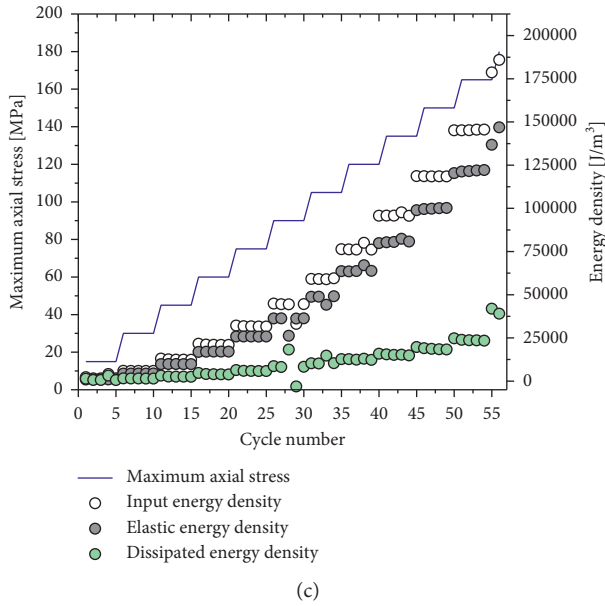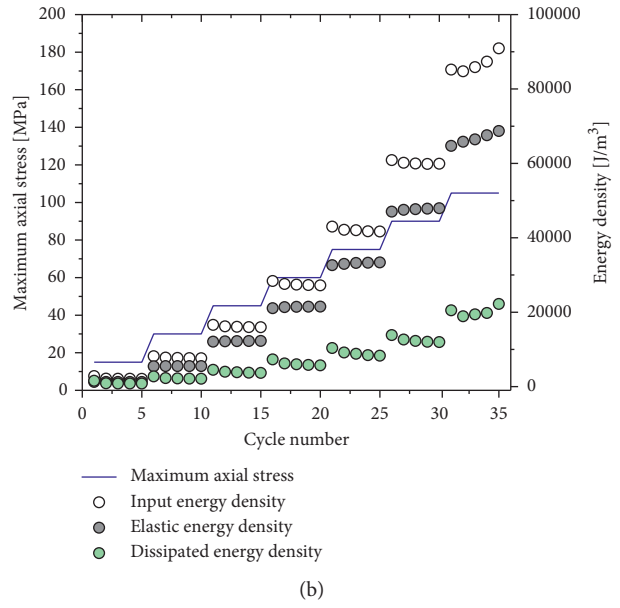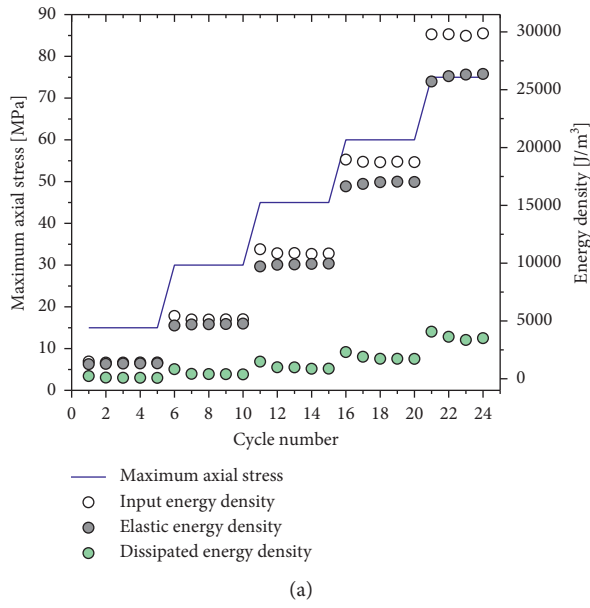
(a)

(b)

(c)

(d)
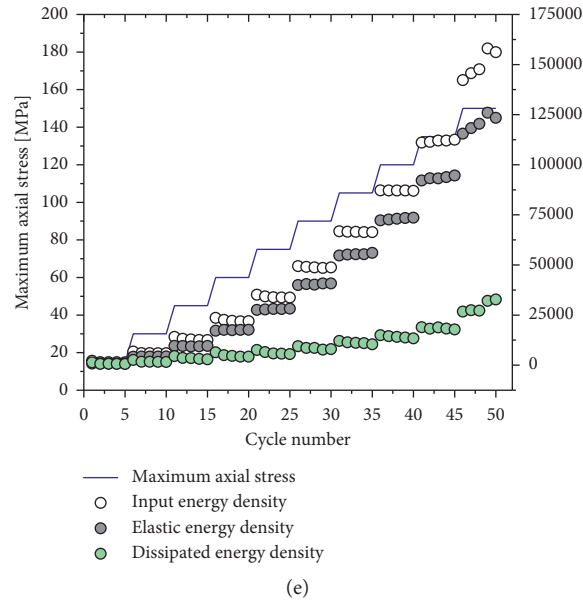
FIGURE 15: Continued.

(e)

FIGURE 15: Evolution of energy densities under triaxial cyclic loading. (a) #6, no confinement. (b) #13, confinement 10 MPa. (c) #14, confinement 15 MPa. (d) #15, confinement 20 MPa. (e) #16, confinement 25 MPa.
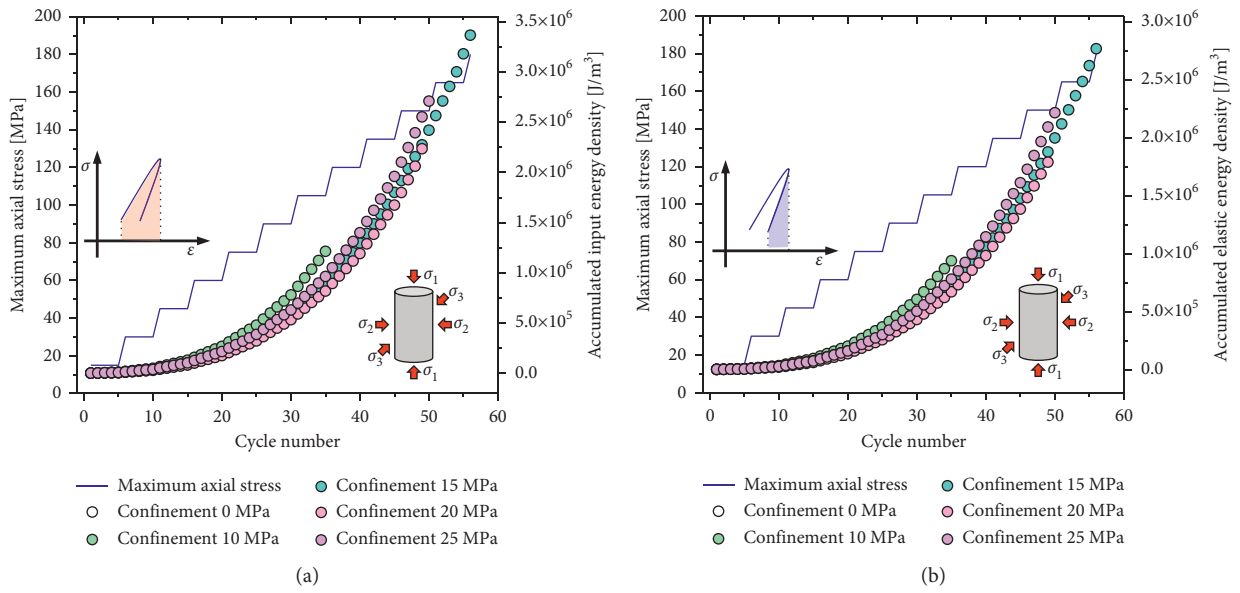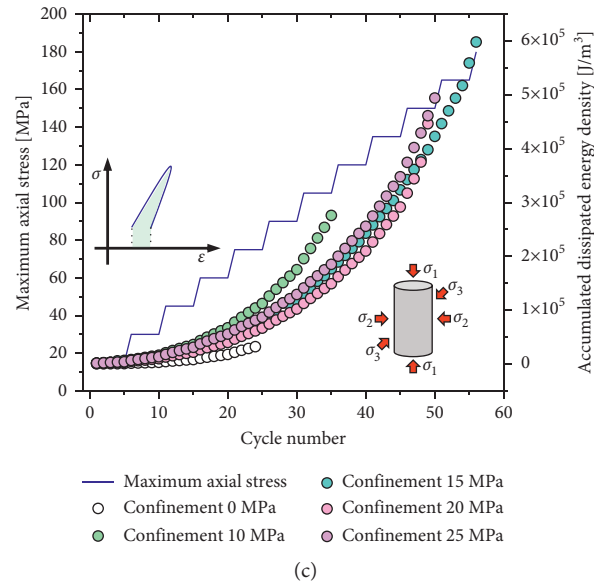

(a)

(b)

FIGURE 16: Continued.

(c)

FIGURE 16: Evolution of accumulated energy densities under triaxial cyclic loading. (a) accumulated input energy density; (b) accumulated elastic energy density; (c) accumulated dissipated energy density.

the impact of the confinement on energy density is not pronounced in triaxial cyclic loading. The general patterns of all three types of energy exposed to different levels of confinement are quite similar and highly consistent. A lower confinement (0 and 10 MPa) causes a smaller amount of accumulated energy density at failure (see Figure 16). To sum up, amplitudes of confining pressures have limited or at least unpronounced impact on the evolution pattern of all three types of accumulated energy density under triaxial cyclic loading. However, the level of confining pressure determines the amount of total accumulated energy density at failure. Lower confining pressure leads to a smaller amount of energy exchange during triaxial cyclic loading, which is characterized by lower levels of all three types of energy density.

4. Stress-Strain Phase Shift during Cyclic Loading

A phase shift between stress and strain of rocklike materials exposed to cyclic loading at the lab scale is already documented [23, 69, 70]. Zhang et al. [23] state that the stress-strain phase shift during cyclic loading of brittle geomaterials can be categorized into four modes as shown in Figure 17. The phase shift analysis is performed at the peak stress within one cycle. Point A and point B in Figure 17 indicate maximum axial stress and maximum axial strain within a cycle. When B appears earlier than A, or A and B simultaneously occur, the material behaves as being perfectly elastic. If B lags behind A (maximum stress appears prior to maximum strain), inelasticity occurs. Usually, increasing stress level causes the more pronounced phase shift (larger lag time). Close to the macroscopic rupture (last cycle preceding failure), the lag time can be infinite, which signifies the complete loss of stiffness and load bearing capacity.

For illustrating the axial stress-axial strain phase shift, we define the following: if maximum axial strain precedes maximum axial stress within a cycle, the phase shift is negative, and vice versa. Therefore, a larger positive phase shift always indicates a higher degree of damage.

The value of phase shift versus cycle number for samples subjected to unconfined cyclic loading is plotted in Figure 18. The phase shift of the last cycle just before failure is excluded due to the infinite value. Figures 18(a), 18(b), and 18(e) show that the phase shift drastically grows when approaching failure. This specific behaviour was also detected before in uniaxial cyclic tests on soft and low-strength (UCS around 20 MPa) materials such as plain concrete [71] and coal [23]. However, as shown by Figures 18(c) and 18(d), no dramatic increase of phase shift is captured prior to failure, which demonstrates that this parameter may not be an appropriate and reliable failure precursor for hard brittle rocks. The marked green columns in Figure 18 indicate the simultaneous increase of axial stress and phase shift and signify that a stepwise increase of stress is always associated with a sudden increase of phase shift under uniaxial cyclic loading. The new damage induced by stress increment can be well characterized by the corresponding rise in phase shift.

The results of stress-strain phase shift during cyclic loading considering different confinements are presented in Figure 19. Apart from Figure 19(a), which represents the unconfined loading scenario for comparison, all other cases exhibit a growth in phase shift immediately preceding the failure. This increase may not be the largest overall; for example, as shown in Figures 19(d) and 19(e), the largest value of phase shift happens much earlier, which indicates a serious damage at that time. It seems that confining pressure increases the phase shift compared to unconfined cyclic loading. Furthermore, the rise of phase shift with increasing load level is more frequently noticed, as indicated by the green columns in Figure 19. Confinement makes phase shifts for samples
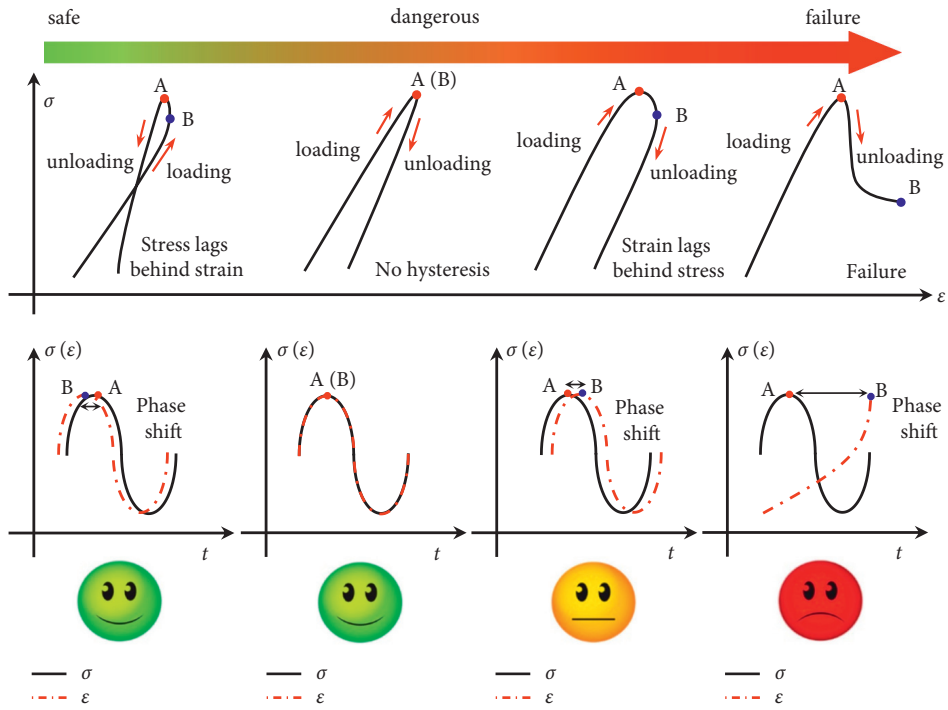
FIGURE 17: Stress-strain phase shift during cyclic loading, reproduced from [23].
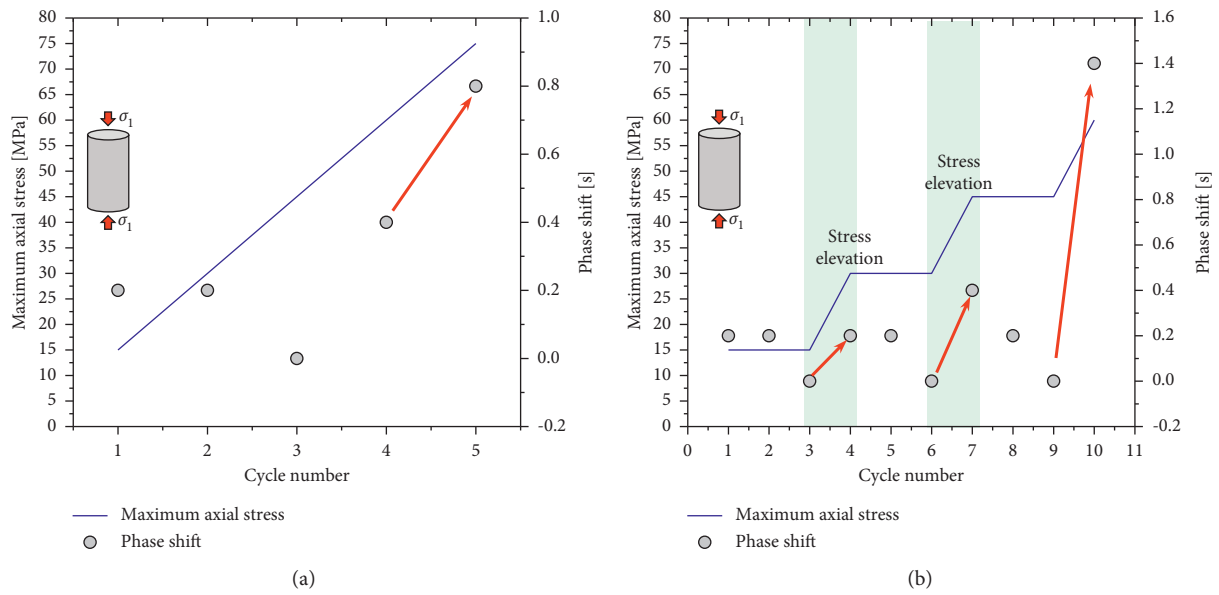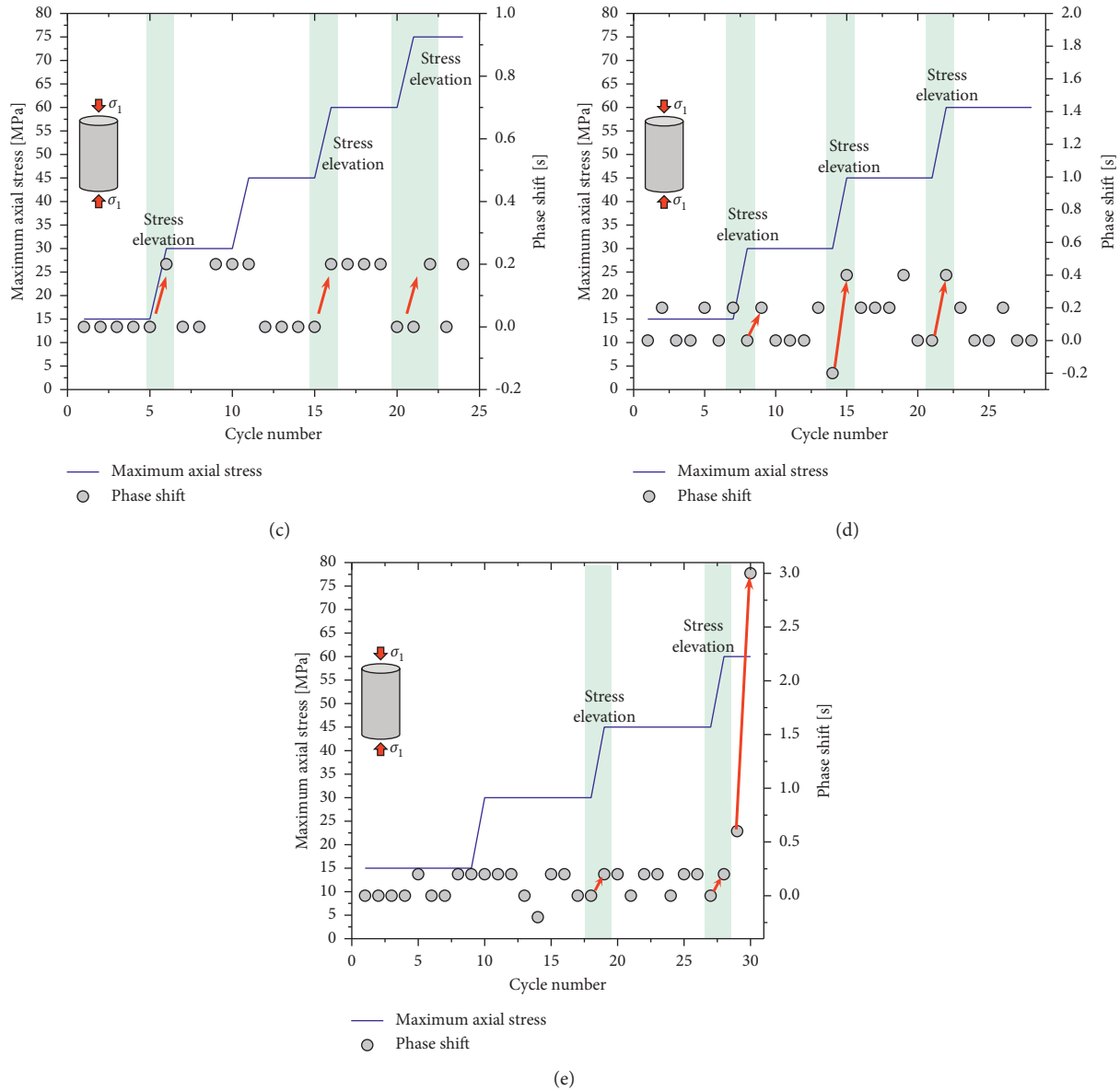

(a)

(b)

FIGURE 18: Continued.

(c)

(d)

(e)

FIGURE 18: Stress-strain phase shift during uniaxial cyclic loading. (a) #4, 1 cycle in each level. (b) #5, 3 cycles in each level. (c) #6, 5 cycles in each level. (d) #7, 7 cycles in each level. (e) #8, 9 cycles in each level.

more sensitive to variations in stress levels than under uniaxial cyclic loading. Figure 19(f) presents the quantitative correlation between confining pressures and average phase shift based on the data sets presented in Figures 19(a)–19(e). A highly linear relation is found between average phase shift and confining pressure. This suggests that a larger confining pressure applied in cyclic loading will result in a more obvious stress-strain phase shift. A corresponding interpretation can be performed by considering energy exchange and dilation. Confining pressure allows a more robust energy exchange and a much larger dilation compared to unconfined cyclic loading. Dilatancy and large amount of energy dissipation during triaxial cyclic loading can exacerbate the stress-strain hysteresis, which results in a larger phase shift. The stress-strain phase shift is a typical behavior concerning hysteresis [72],

and many mechanical and environmental parameters can influence the extent of phase shift for rocks, such as loading frequency [23], effect of fluid [69], stress level [67], temperature [73], and structures of material. In this work, the average phase shift is more pronounced when the confinement is used. This can be interpreted from the viscoplastic behaviors of rocks. The loading rate and temperature remain constant, and the effect of fluid is not considered. The application of confinement is the unique factor to make the rock sample withstand more plastic strain and more fractures prior to final failure. The phase shift is sensitive to the fracture evolution, and the periodic closure and opening of the fractures are mainly responsible for the phase shift. Therefore, more fractures are generated, and the effect induced by the closure and opening of the fractures is more dominant. This
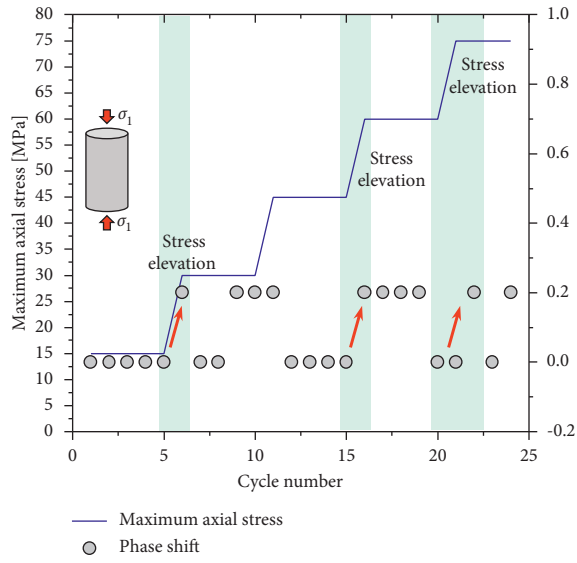
(a)
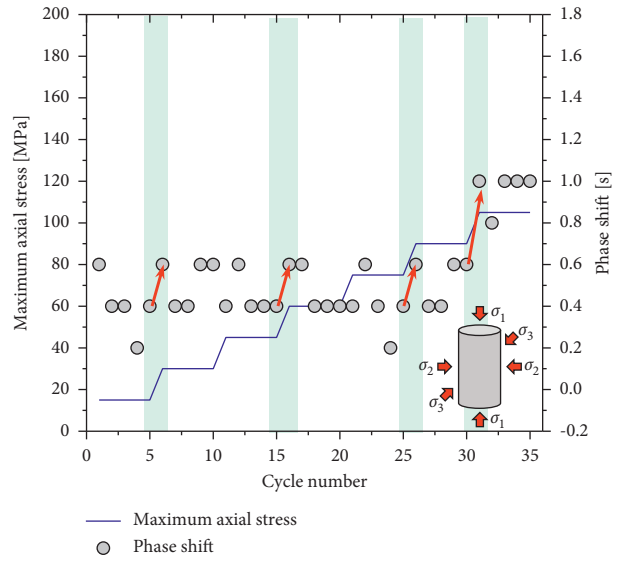
(b)
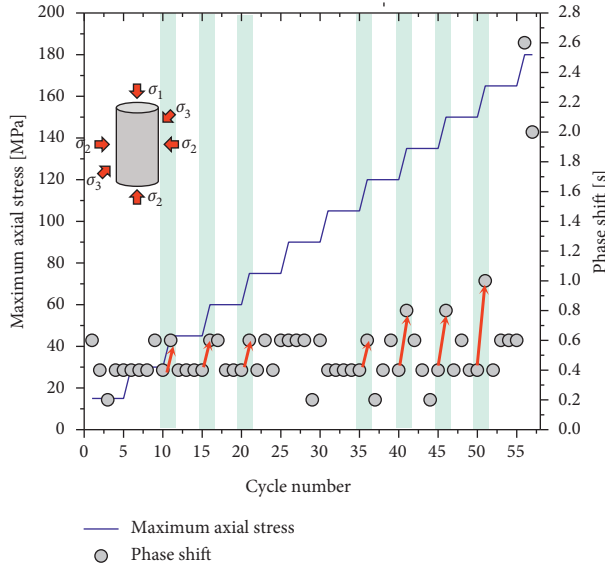
(c)

(d)

Figure 19: Continued.

(e)

(f)

FIGURE 19: Stress-strain phase shift during triaxial cyclic loading. (a) #6, no confinement. (b) #13, confinement of 10 MPa. (c) #14, confinement of 15 MPa. (d) #15, confinement of 20 MPa. (e) #16, confinement of 25 MPa. (f) Fitting of confining pressure vs. average phase shift.

TABLE 2: Physical and mechanical properties of granite samples.

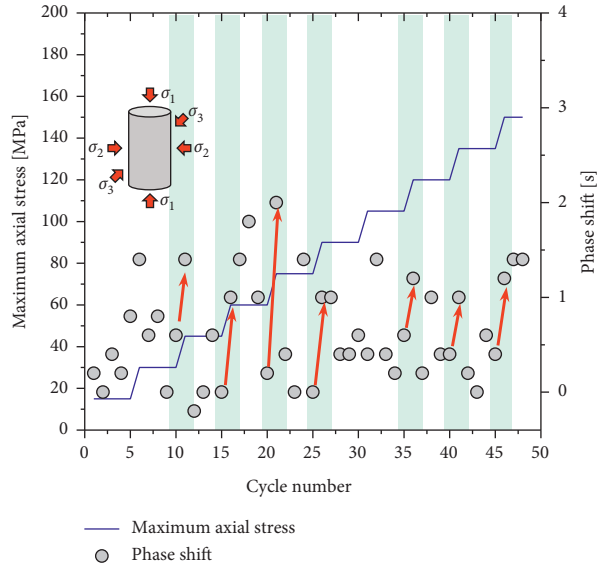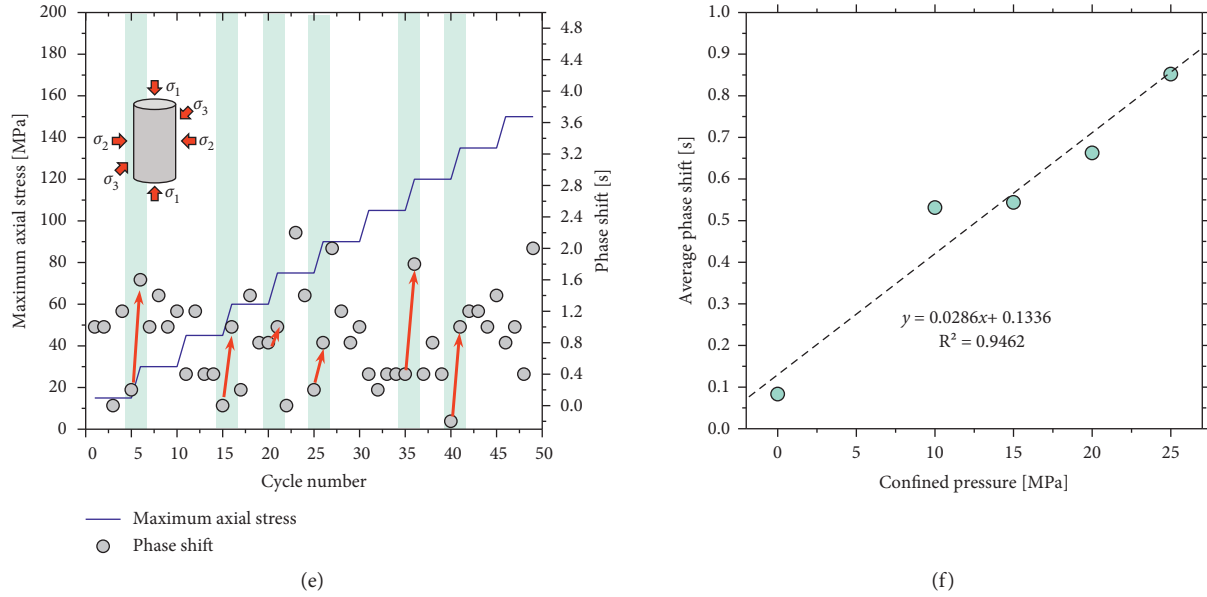| Samples Unit	P-wave velocity (m/s)	Height (mm)	Diameter (mm)	Mass (g)	Density (g/cm^3)	Stress state [—]	Loading regime [—]
#1	4634	99.93	50.14	512	2.608	Uniaxial	Monotonic
#2	4568	99.85	50.06	527	2.684	Uniaxial	Monotonic
#3	4586	99.98	50.21	524	2.669	Uniaxial	Monotonic
#4	4611	99.99	50.09	524	2.648	Uniaxial	Cyclic
#5	4597	100.05	49.99	527	2.614	Uniaxial	Cyclic
#6	4627	100.08	50.00	518	2.649	Uniaxial	Cyclic
#7	4749	99.85	50.11	522	2.684	Uniaxial	Cyclic
#8	4641	99.97	50.06	524	2.649	Uniaxial	Cyclic
#9	4535	100.05	50.02	534	2.665	Triaxial	Monotonic
#10	4668	99.98	49.96	525	2.624	Triaxial	Monotonic
#11	4786	100.04	50.15	519	2.675	Triaxial	Monotonic
#12	4655	100.01	50.00	522	2.667	Triaxial	Monotonic
#13	4630	99.97	50.13	537	2.618	Triaxial	Cyclic
#14	4863	100.02	50.24	522	2.637	Triaxial	Cyclic
#15	4749	99.96	50.11	525	2.629	Triaxial	Cyclic
#16	4675	99.91	50.20	534	2.645	Triaxial	Cyclic

has been proved with the aid of acoustic emission measurement in our former work [23, 67]. This is also related to the rock dilation, and the larger the confinement can result in a more pronounced rock dilation, the larger the rock dilation is associated with the more shear fractures and occurrence of grain sliding; this will also cause a more pronounced plasticity, which can intensify the phase shift.

Table 2 lists physical and mechanical properties of granites samples prepared for laboratory testing. P-wave velocities are measured along the axial direction before testing. In total, 16 granite samples with similar P-wave velocities are selected to conduct uniaxial and triaxial tests (see Table 2).

5. Conclusions

This work presents experimental investigations on the mechanical behavior of granite samples from great depth (−915 m) exposed to the uniaxial and triaxial monotonic and cyclic loading. Test results are evaluated considering compressive strength, strain evolution, energy exchange, and stress-strain hysteresis. The following conclusions are drawn:

(1) The granite samples failed in a contraction pattern when subjected to the unconfined compression in both monotonic and cyclic loading regimes. Significant dilatancy is observed under confined

compression in both monotonic and cyclic loading regimes. The increase of confining pressures reduces the stress ratio (axial stresses at minimum volume and onset of dilatancy to compressive strength) in both triaxial monotonic and cyclic tests, which indicate that dilation will appear earlier under higher confinement under monotonic as well cyclic loading.

(2) Confining pressure leads to larger axial and radial strain at failure compared to unconfined loading scenarios. Lower confining pressure induces a higher growth rate of axial strain, whereas the effect of confinement on radial strain is not pronounced. Under uniaxial cyclic loading, the secant elastic modulus shows a stepwise increase with the increase of axial stress and a sharp decline appears prior to failure. Under triaxial cyclic loading, high confining pressure (larger than 20 MPa) leads to a monotonic degradation of secant modulus regardless of the variations of the axial stress.

(3) Evolution of input, elastic recovery, and dissipated energy density all show a high consistency when the stress path is fixed in triaxial cyclic loading. The confining pressure impacts the amount of total energy exchange at failure, but not the general pattern. A higher confinement allows a more violent exchange of energy during the cyclic loading, which is characterized by a large amount of accumulated energy at failure.

(4) Under uniaxial cyclic loading, the evolution of stress-strain phase shift prior to failure exhibits two different patterns: either sudden growth or no growth. However, under triaxial cyclic loading, an abrupt rise of phase shift preceding failure is prominent due to the application of confining pressure. Test results show that the average phase shift is proportional to the applied confined pressure under triaxial cyclic loading.

Data Availability

The data are available upon request.

Conflicts of Interest

The authors declare that there are no conflicts of interest regarding this work.

Acknowledgments

References

[1] Z. Song, H. Konietzky, and M. Herbst, "Drawing mechanism of fractured top coal in longwall top coal caving," *International Journal of Rock Mechanics and Mining Sciences*, vol. 130, Article ID 104329, 2020.

[2] Z. Song, T. Frühwirt, and H. Konietzky, "Fatigue characteristics of concrete subjected to indirect cyclic tensile loading: insights from deformation behavior, acoustic emissions and ultrasonic wave propagation," *Construction and Building Materials*, vol. 302, Article ID 124386, 2021.

[3] R. Shirani Faradonbeh, A. Taheri, and M. Karakus, "Post-peak behaviour of rocks under cyclic loading using a double-criteria damage-controlled test method," *Bulletin of Engineering Geology and the Environment*, vol. 80, no. 2, pp. 1713–1727, 2021.

[4] W. Dang, H. Konietzky, T. Frühwirt, and M. Herbst, "Cyclic frictional responses of planar joints under cyclic normal load conditions: laboratory tests and numerical simulations," *Rock Mechanics and Rock Engineering*, vol. 53, 2019.

[5] W. Chen, H. Konietzky, C. Liu, and X. Tan, "Hydraulic fracturing simulation for heterogeneous granite by discrete element method," *Computers and Geotechnics*, vol. 95, pp. 1–15, 2018.

[6] Y. Liu, F. Dai, L. Dong, N. Xu, and P. Feng, "Experimental investigation on the fatigue mechanical properties of intermittently jointed rock models under cyclic uniaxial compression with different loading parameters," *Rock Mechanics and Rock Engineering*, vol. 51, no. 1, pp. 47–68, 2018.

[7] Z. Song, H. Konietzky, and M. Herbst, "Three-dimensional particle model based numerical simulation on multi-level compressive cyclic loading of concrete," *Construction and Building Materials*, vol. 225, pp. 661–677, 2019.

[8] Z. Song and H. Konietzky, "A particle-based numerical investigation on longwall top coal caving mining," *Arabian Journal of Geosciences*, vol. 12, no. 18, p. 556, 2019.

[9] E. C. David, N. Brantut, A. Schubnel, and R. W. Zimmerman, "Sliding crack model for nonlinearity and hysteresis in the uniaxial stress-strain curve of rock," *International Journal of Rock Mechanics and Mining Sciences*, vol. 52, pp. 9–17, 2012.

[10] J. E. Kendrick, R. Smith, P. Sammonds, P. G. Meredith, M. Dainty, and J. S. Pallister, "The influence of thermal and cyclic stressing on the strength of rocks from Mount St. Helens, Washington," *Bulletin of Volcanology*, vol. 75, no. 7, p. 728, 2013.

[11] M. J. Heap, S. Vinciguerra, and P. G. Meredith, "The evolution of elastic moduli with increasing crack damage during cyclic stressing of a basalt from Mt. Etna volcano," *Tectonophysics*, vol. 471, no. 1-2, pp. 153–160, 2009.

[12] Z. Song, H. Konietzky, and X. Cai, "Modulus degradation of concrete exposed to compressive fatigue loading: insights from lab testing," *Structural Engineering & Mechanics*, vol. 78, pp. 281–296, 2021.

[13] D. V. Okur and A. Ansal, "Stiffness degradation of natural fine grained soils during cyclic loading," *Soil Dynamics and Earthquake Engineering*, vol. 27, no. 9, pp. 843–854, 2007.

[14] W. Dang, H. Konietzky, and T. Frühwirt, "Direct shear behavior of a plane joint under dynamic normal load (DNL) conditions," *Engineering Geology*, vol. 213, pp. 133–141, 2016.

[15] Z. Song, T. Frühwirt, and H. Konietzky, "Inhomogeneous mechanical behaviour of concrete subjected to monotonic and cyclic loading," *International Journal of Fatigue*, vol. 132, Article ID 105383, 2020.

[16] R. K. Dowell, F. Seible, and E. L. Wilson, "Pivot hysteresis model for reinforced concrete members," *ACI Structural Journal*, vol. 95, pp. 607–617, 1998.

[17] R. Geranmayeh Vaneghi, B. Ferdosi, A. D. Okoth, and B. Kuek, "Strength degradation of sandstone and granodiorite under uniaxial cyclic loading," *Journal of Rock Mechanics and Geotechnical Engineering*, vol. 10, no. 1, pp. 117–126, 2018.

[18] H. Liu, K. Gao, and X. Zhu, "Experimental study on dynamic fatigue properties of dolomite samples under triaxial multi-level cyclic loading," *Bulletin of Engineering Geology and the Environment*, vol. 80, no. 1, pp. 551–565, 2021.

[19] Z. Song, H. Konietzky, and M. Herbst, "Bonded-particle model-based simulation of artificial rock subjected to cyclic loading," *Acta Geotechnica*, vol. 14, no. 4, pp. 955–971, 2019.

[20] M. N. Bagde and V. Petroš, "Fatigue properties of intact sandstone samples subjected to dynamic uniaxial cyclical loading," *International Journal of Rock Mechanics and Mining Sciences*, vol. 42, no. 2, pp. 237–250, 2005.

[21] G. Su, L. Hu, X. Feng et al., "True triaxial experimental study of rockbursts induced by ramp and cyclic dynamic disturbances," *Rock Mechanics and Rock Engineering*, vol. 51, no. 4, pp. 1027–1045, 2018.

[22] X. Cai, Z. Zhou, L. Tan, H. Zang, and Z. Song, "Fracture behavior and damage mechanisms of sandstone subjected to wetting-drying cycles," *Engineering Fracture Mechanics*, vol. 234, Article ID 107109, 2020.

[23] M. Zhang, L. Dou, H. Konietzky, Z. Song, and S. Huang, "Cyclic fatigue characteristics of strong burst-prone coal: experimental insights from energy dissipation, hysteresis and micro-seismicity," *International Journal of Fatigue*, vol. 133, Article ID 105429, 2020.

[24] Z.-l. Li, X.-q. He, L.-m. Dou, D.-z. Song, G.-f. Wang, and X.-l. Xu, "Investigating the mechanism and prevention of coal mine dynamic disasters by using dynamic cyclic loading tests," *Safety Science*, vol. 115, pp. 215–228, 2019.

[25] P. Li, X. Feng, G. Feng, Y. Xiao, and B. Chen, "Rockburst and microseismic characteristics around lithological interfaces under different excavation directions in deep tunnels," *Eng Geol*, vol. 260, Article ID 105209, 2019.

[26] L. N. Y. Wong, V. S. K. Lai, and T. P. Y. Tam, "Joint spacing distribution of granites in Hong Kong," *Engineering Geology*, vol. 245, pp. 120–129, 2018.

[27] L. N. Y. Wong, T. Y. Guo, W. K. Lam, and J. Y. H. Ng, "Experimental study of cracking characteristics of kowloon granite based on three mode I fracture toughness methods," *Rock Mechanics and Rock Engineering*, vol. 52, no. 11, pp. 4217–4235, 2019.

[28] B. J. Brennan and F. D. Stacey, "Frequency dependence of elasticity of rock-test of seismic velocity dispersion," *Nature*, vol. 268, no. 5617, pp. 220–222, 1977.

[29] S. Wang, L. Huang, and X. Li, "Analysis of rockburst triggered by hard rock fragmentation using a conical pick under high uniaxial stress," *Tunnelling and Underground Space Technology*, vol. 96, Article ID 103195, 2020.

[30] Q. B. Zhang and J. Zhao, "A review of dynamic experimental techniques and mechanical behaviour of rock materials," *Rock Mechanics and Rock Engineering*, vol. 47, no. 4, pp. 1411–1478, 2014.

[31] B. Cerfontaine and F. Collin, "Cyclic and fatigue behaviour of rock materials: review, interpretation and research perspectives," *Rock Mechanics and Rock Engineering*, vol. 51, no. 2, pp. 391–414, 2018.

[32] J. Zhao, G. Guo, D. Xu, X. Huang, C. Hu, Y. Xia et al., "Experimental study of deformation and failure characteristics of deeply-buried hard rock under triaxial and cyclic loading and unloading stress paths," *Rock Soil Mech*, vol. 41, pp. 1521–1530, 2020.

[33] Z. Zhou, X. Cai, X. Li, W. Cao, and X. Du, "Dynamic response and energy evolution of sandstone under coupled static-dynamic compression: insights from experimental study into deep rock engineering applications," *Rock Mechanics and Rock Engineering*, vol. 53, no. 3, pp. 1305–1331, 2020.

[34] X. Cai, Z. Zhou, L. Tan, H. Zang, and Z. Song, "Water saturation effects on thermal infrared radiation features of rock materials during deformation and fracturing," *Rock Mechanics and Rock Engineering*, vol. 53, 2020.

[35] X. Cai, Z. Zhou, H. Zang, and Z. Song, "Water saturation effects on dynamic behavior and microstructure damage of sandstone: phenomena and mechanisms," *Engineering Geology*, vol. 276, Article ID 105760, 2020.

[36] K. Peng, J. Zhou, Q. Zou, and F. Yan, "Deformation characteristics of sandstones during cyclic loading and unloading with varying lower limits of stress under different confining pressures," *International Journal of Fatigue*, vol. 127, pp. 82–100, 2019.

[37] J. Fan, J. Chen, D. Jiang, S. Ren, and J. Wu, "Fatigue properties of rock salt subjected to interval cyclic pressure," *International Journal of Fatigue*, vol. 90, pp. 109–115, 2016.

[38] M. Ghamgosar, N. Erarslan, and D. J. Williams, "Experimental investigation of fracture process zone in rocks damaged under cyclic loadings," *Experimental Mechanics*, vol. 57, no. 1, pp. 97–113, 2017.

[39] E. Liu and S. He, "Effects of cyclic dynamic loading on the mechanical properties of intact rock samples under confining pressure conditions," *Engineering Geology*, vol. 125, pp. 81–91, 2012.

[40] S.-Q. Yang, Y.-H. Huang, and J.-Z. Tang, "Mechanical, acoustic, and fracture behaviors of yellow sandstone specimens under triaxial monotonic and cyclic loading," *International Journal of Rock Mechanics and Mining Sciences*, vol. 130, Article ID 104268, 2020.

[41] T. M. Mitchell and D. R. Faulkner, "Experimental measurements of permeability evolution during triaxial compression of initially intact crystalline rocks and implications for fluid flow in fault zones," *Journal of Geophysical Research Atmospheres*, vol. 113, Article ID B11412, 2008.

[42] P. K. Kaiser and M. Cai, "Design of rock support system under rockburst condition," *Journal of Rock Mechanics and Geotechnical Engineering*, vol. 4, no. 3, pp. 215–227, 2012.

[43] L. Hu, K. Ma, X. Liang, C. Tang, Z. Wang, and L. Yan, "Experimental and numerical study on rockburst triggered by tangential weak cyclic dynamic disturbance under true triaxial conditions," *Tunnelling and Underground Space Technology*, vol. 81, pp. 602–618, 2018.

[44] X. Li, C. Liu, S. S. Peng, and Y. Lu, "Fatigue deformation characteristics and damage model of sandstone subjected to uniaxial step cyclic loading," *Journal of China University of Mining and Technology*, vol. 46, pp. 8–17, 2017.

[45] Y. Zhou, S. Su, and H. Ma, "Experimental research on elastic modulus evolution of chlorite phyllite under cyclic loading," *J Cent South Univ (Science Technol*, vol. 51, pp. 783–792, 2020.

[46] S. Yang, Y. Tao, and J. Tang, "Experimental study on triaxial strength and deformation of single jointed sandstone under cyclic loading," *Journal of China University of Mining and Technology*, vol. 49, pp. 819–825, 2020.

[47] Y. Wei, C. Yang, Y. Guo, and W. Liu, "Experimental research on deformation and fracture characteristics of shale under cyclic loading," *Chinese Journal of Geotechnical Engineering*, vol. 37, pp. 2262–2271, 2015.

[48] C. Su, Z. Xiong, X. Zhai, and M. Gu, "Analysis of deformation and strength characteristics of coal samples under the triaxial cyclic loading and unloading stress path," *J Min Saf Eng*, vol. 31, pp. 456–461, 2014.

[49] T. Li, Y. Ma, B. Liu, H. Sheng, and P. He, "Strength characteristics and elastic modulus evolution of frozen gray sandstone under cyclic loading," *Journal of China Coal Society*, vol. 43, pp. 2438–2443, 2018.

[50] A. E. Aladejare, "Evaluation of empirical estimation of uniaxial compressive strength of rock using measurements from index and physical tests," *Journal of Rock Mechanics and Geotechnical Engineering*, vol. 12, no. 2, pp. 256–268, 2020.

[51] A. Rouabhi, P. Labaune, M. Tijani, N. Gatelier, and G. Hévin, "Phenomenological behavior of rock salt: on the influence of laboratory conditions on the dilatancy onset," *Journal of Rock Mechanics and Geotechnical Engineering*, vol. 11, no. 4, pp. 723–738, 2019.

[52] X. Zhao, M. Cai, and M. Cai, "Considerations of rock dilation on modeling failure and deformation of hard rocks—a case study of the mine-by test tunnel in Canada," *Journal of Rock Mechanics and Geotechnical Engineering*, vol. 2, pp. 338–349, 2010.

[53] X. G. Zhao and M. Cai, "Influence of plastic shear strain and confinement-dependent rock dilation on rock failure and displacement near an excavation boundary," *International Journal of Rock Mechanics and Mining Sciences*, vol. 47, no. 5, pp. 723–738, 2010.

[54] H. Alkan, Y. Cinar, and G. Pusch, "Rock salt dilatancy boundary from combined acoustic emission and triaxial compression tests," *International Journal of Rock Mechanics and Mining Sciences*, vol. 44, no. 1, pp. 108–119, 2007.

[55] N. Bahrani and P. K. Kaiser, "Influence of degree of interlock on confined strength of jointed hard rock masses," *Journal of Rock Mechanics and Geotechnical Engineering*, vol. 12, no. 6, pp. 1152–1170, 2020.

[56] J.-Q. Xiao, D.-X. Ding, F.-L. Jiang, and G. Xu, "Fatigue damage variable and evolution of rock subjected to cyclic loading," *International Journal of Rock Mechanics and Mining Sciences*, vol. 47, no. 3, pp. 461–468, 2010.

[57] P. B. Attewell and I. W. Farmer, "Fatigue behaviour of rock," *International Journal of Rock Mechanics and Mining Science & Geomechanics Abstracts*, vol. 10, no. 1, pp. 1–9, 1973.

[58] P. Ameen and M. Szymanski, "Fatigue in plain concrete: phenomenon and methods of analysis," *ACI J Proc*, 2006.

[59] I. M. Idriss, Y. Moriwaki, S. G. Wright, E. H. Doyle, and R. S. Ladd, "Behavior of normally consolidated clay under simulated earthquake and ocean wave loading conditions," *Int. Symp. soils under Cycl. transient Load.*vol. 1, pp. 437–445, 1980.

[60] S. Tang, C. Yu, and C. Tang, "Numerical modeling of the time-dependent development of the damage zone around a tunnel under high humidity conditions," *Tunnelling and Underground Space Technology*, vol. 76, pp. 48–63, 2018.

[61] T.-S. Eom, H.-G. Park, and S.-M. Kang, "Energy-based cyclic force-displacement relationship for reinforced concrete short coupling beams," *Engineering Structures*, vol. 31, no. 9, pp. 2020–2031, 2009.

[62] D. Song, E. Wang, and J. Liu, "Relationship between EMR and dissipated energy of coal rock mass during cyclic loading process," *Safety Science*, vol. 50, no. 4, pp. 751–760, 2012.

[63] Q. Meng, M. Zhang, L. Han, H. Pu, and T. Nie, "Effects of acoustic emission and energy evolution of rock specimens under the uniaxial cyclic loading and unloading compression," *Rock Mechanics and Rock Engineering*, vol. 49, 2016.

[64] Z. Song, T. Frühwirt, and H. Konietzky, "Characteristics of dissipated energy of concrete subjected to cyclic loading," *Construction and Building Materials*, vol. 168, pp. 47–60, 2018.

[65] K. A. Ghuzlan and S. H. Carpenter, "Fatigue damage analysis in asphalt concrete mixtures using the dissipated energy approach," *Canadian Journal of Civil Engineering*, vol. 33, no. 7, pp. 890–901, 2006.

[66] M. He, N. Li, C. Zhu, Y. Chen, and H. Wu, "Experimental investigation and damage modeling of salt rock subjected to fatigue loading," *International Journal of Rock Mechanics and Mining Sciences*, vol. 114, pp. 17–23, 2019.

[67] Z. Song, Y. Wang, H. Konietzky, and X. Cai, "Mechanical behavior of marble exposed to freeze-thaw-fatigue loading," *International Journal of Rock Mechanics and Mining Sciences*, vol. 138, Article ID 104648, 2021.

[68] A. M. Korsunsky, D. Dini, F. P. E. Dunne, and M. J. Walsh, "Comparative assessment of dissipated energy and other fatigue criteria," *International Journal of Fatigue*, vol. 29, 2007.

[69] D. Xi, Y. Chen, Y. Tao, and Y. Liu, "Nonlinear elastic hysteric characteristics of rocks," *Chinese Journal of Rock Mechanics and Engineering*, vol. 25, pp. 1086–1093, 2006.

[70] Z. Song, H. Konietzky, and T. Frühwirt, "Hysteresis energy-based failure indicators for concrete and brittle rocks under the condition of fatigue loading," *International Journal of Fatigue*, vol. 114, pp. 298–310, 2018.

[71] Z. Song, H. Konietzky, and T. Frühwirt, "Hysteresis and dynamic response features of concrete exposed to repeated multilevel compressive loading," *Journal of Materials in Civil Engineering*, vol. 31, Article ID 04019066, 2019.

[72] D. S. Schmool and D. Markó, "Magnetism in solids: hysteresis," *Reference Module in Materials Science and Materials Engineering*, Elsevier, Amsterdam, Netherlands, 2018.

[73] J.-h. Zhang, J. Wang, and L.-s. Chai, "Factors influencing hysteresis characteristics of concrete dam deformation," *Water Science and Engineering*, vol. 10, no. 2, pp. 166–174, 2017.